



# A framework for triple oxygen isotopes in speleothem paleoclimatology

Tyler E. Huth<sup>a,\*</sup>, Benjamin H. Passey<sup>a</sup>, Julia E. Cole<sup>a</sup>, Matthew S. Lachniet<sup>b</sup>, David McGee<sup>c</sup>, Rhawn F. Denniston<sup>d</sup>, Sarah Truebe<sup>e</sup>, Naomi E. Levin<sup>a</sup>

<sup>a</sup> Department of Earth and Environmental Sciences, University of Michigan, Ann Arbor, MI 48109, USA

<sup>b</sup> Department of Geoscience, University of Nevada, Las Vegas, Las Vegas, NV 89154, USA

<sup>c</sup> Department of Earth, Atmospheric, and Planetary Sciences, Massachusetts Institute of Technology, Cambridge, MA 02139, USA

<sup>d</sup> Department of Geology, Cornell College, Mount Vernon, Iowa 52314, USA

<sup>e</sup> Department of Geosciences, University of Arizona, Tucson, AZ 85721, USA

Received 25 March 2021; accepted in revised form 2 November 2021; available online xxxx

## Abstract

Speleothem oxygen isotope ( $\delta^{18}\text{O}$ ) records provide key insight into the rate and timing of terrestrial paleoclimate changes during the late Quaternary. However, it can be difficult to deconvolve the  $\delta^{18}\text{O}$  signal into individual components, which include processes related to moisture source, moisture transport, temperature, precipitation amount, infiltration, and the cave environment. We developed a framework that uses triple oxygen isotope distributions in speleothems to refine interpretations of  $\delta^{18}\text{O}$  speleothem records. This framework identifies the influence of dominant processes on  $\delta^{18}\text{O}$  values through time by their characteristic (although not necessarily unique) trends in  $\Delta^{17}\text{O}$  vs.  $\delta^{18}\text{O}$  space, where  $\Delta^{17}\text{O} = \delta^{17}\text{O} - 0.528\delta^{18}\text{O}$  and  $\delta^{x}\text{O} = \ln(\delta^{x}\text{O} + 1)$ . Following Guo and Zhou (2019a), we expect that ‘cave kinetic’ processes (e.g., fast degassing at the drip site, prior calcite precipitation) will drive positive trends between  $\delta^{18}\text{O}$  and  $\Delta^{17}\text{O}$ . In contrast, we can identify hydrologic processes from near-horizontal trends that reflect Rayleigh-type meteoric water processes and negative trends driven by changes in evaporation processes at the moisture source region or at the cave site, mineralization temperature, and seasonality in precipitation/infiltration amount. We applied this framework to four western USA speleothems from Cave of the Bells (Arizona), Leviathan Cave (Nevada), and Lehman Caves (Nevada). The Cave of the Bells and Leviathan data have near-horizontal to negative trends indicating  $\delta^{18}\text{O}$  variability was driven largely by changes in Rayleigh distillation of atmospheric moisture and moisture source conditions, supporting prior interpretations. We analyzed two Lehman Caves records because they were likely influenced by non-equilibrium processes and the data show weak to moderate negative trends. For sample LMC-12b, chosen for its extreme 7.5‰  $\delta^{18}\text{O}$  range, the trend is statistically distinct from the near-horizontal Rayleigh-process trend and most consistent with changes in local evaporation intensity and infiltration seasonality as primary drivers. None of these records displays a positive covariation slope between  $\delta^{18}\text{O}$  and  $\Delta^{17}\text{O}$ , suggesting limited variability in cave kinetic processes through time or unknown limitations to the kinetic model of Guo and Zhou (2019a). Additionally, reconstructed formation waters for all sites fall near the  $\Delta^{17}\text{O}$  vs.  $\delta^{18}\text{O}$  Local Meteoric Water Line, a correlation we suggest as a novel test of the absolute magnitude of isotopic offset due to cave kinetic processes. More broadly, our framework adds context to the only other study of carbonate speleothem triple oxygen isotope composition (Sha et al., 2020). We find that positive

\* Corresponding author.

E-mail address: [tehuth@umich.edu](mailto:tehuth@umich.edu) (T.E. Huth).

to negative  $\Delta^{17}\text{O}$  vs.  $\delta^{18}\text{O}$  trends likely exist in speleothem data that may reasonably be expected from regional climate processes and that, combined with other proxy data, triple oxygen isotope data will be useful in constraining interpretations of  $\delta^{18}\text{O}_{\text{speleothem}}$  records.

© 2021 Elsevier Ltd. All rights reserved.

**Keywords:** Triple oxygen isotopes; Carbonate speleothem; Terrestrial paleoclimatology; Meteoric water; Western USA

## 1. INTRODUCTION

### 1.1. Triple oxygen isotope background and previous work

Speleothems are commonly used as archives for past changes in Earth's hydrologic cycle because they are suitable for precise U-series dating and their oxygen isotope composition is related to hydrologic processes (Lachniet, 2009; Cheng et al., 2012; Wong & Breecker, 2015). They provide high-resolution paleoclimate records that have been instrumental in elucidating the rate and timing of the terrestrial response to late Quaternary climate change (Wang et al., 2001; Wagner et al., 2010; Lachniet et al., 2014; Wang et al., 2017). Traditionally, the use of oxygen isotopes in paleoclimate reconstruction has relied on the relative abundance of  $^{18}\text{O}$  to  $^{16}\text{O}$  in a sample, which can be expressed in "delta notation" as:

$$\delta^{18}\text{O} = \frac{R_{\text{sample}}}{R_{\text{standard}}} - 1 \quad (1)$$

where  $R_{\text{sample}}$  and  $R_{\text{standard}}$  represent the  $^x\text{O}/^{16}\text{O}$  ratios of sample and standards (here,  $x = 18$ ). The differences between  $R_{\text{sample}}$  and  $R_{\text{standard}}$  are small for mass-dependent processes occurring at Earth's surface, so their ratio is always close to unity and  $\delta$ -values are generally multiplied by  $10^3$  for convenience (per mil notation, ‰).

Although variability in  $\delta^{18}\text{O}_{\text{speleothem}}$  is generally understood to relate to hydrologic change, identifying the mechanisms of change and their magnitude is not always straightforward. This is because  $\delta^{18}\text{O}_{\text{speleothem}}$  responds to the primary  $\delta^{18}\text{O}_{\text{precipitation}}$  signal, which is itself a function of processes like precipitation seasonality, precipitation intensity, moisture source region, and temperature (Dansgaard, 1964). Patterns of similar magnitude and direction can be produced by different processes, which has resulted in contested interpretations for some records. Additional complexity results from local soil and epikarst processes that affect the  $\delta^{18}\text{O}$  of infiltrating waters and  $\delta^{18}\text{O}_{\text{speleothem}}$ . These include mixing, evaporation, biological processes, prior calcite precipitation along the infiltration path, and changes to the cave environment (e.g., temperature, drip interval, soil/cave  $\text{CO}_2$  concentration, wind speed, relative humidity, mineral formation rate, drip height) (Spötl et al., 2005; Mickler et al., 2006; Baldini et al., 2008; Scholz et al., 2009; Dreybrodt and Scholz, 2011; Deininger et al., 2012; Matthey et al., 2016; Deininger and Scholz, 2019; Hansen et al., 2019).

Thus, while  $\delta^{18}\text{O}_{\text{speleothem}}$  variability may be generally understood to relate to climate change, it can be difficult to demonstrate which process, or processes, created the signal. Attempts to better constrain  $\delta^{18}\text{O}_{\text{speleothem}}$  interpreta-

tions add more information to the system by using, for example, fluid inclusions (McGarry et al., 2004; Affolter et al., 2019), elemental chemistry (Fairchild et al., 2000; Fairchild and Treble, 2009; Steponaitis et al., 2015), trace isotope chemistry (e.g., Richards & Dorale, 2003; Frumkin & Stein, 2004; Musgrove & Banner, 2004; Zhou et al., 2005; Oster et al., 2010; Wong & Banner, 2010) and "clumped" isotope geochemistry (Affek et al., 2008; Daëron et al., 2011; Wainer et al., 2011; Kulge and Affek, 2012; Affek et al., 2014; Affek and Zaarur, 2014). Triple oxygen isotope ( $\Delta^{17}\text{O}$ ) analyses provide additional information to better constrain  $\delta^{18}\text{O}_{\text{speleothem}}$  interpretation (Sha et al., 2020). The  $\Delta^{17}\text{O}$  value, which incorporates information from a sample's  $^{18}\text{O}/^{16}\text{O}$  and  $^{17}\text{O}/^{16}\text{O}$  composition, is the  $^{17}\text{O}$ -excess occurring at a given  $\delta^{18}\text{O}$  value relative to a reference slope (Fig. 1):

$$\Delta^{17}\text{O} = \delta^{17}\text{O} - \lambda_{\text{ref}} \times \delta^{18}\text{O} \quad (2)$$

where "delta-prime" notation is defined as:

$$\delta'^x\text{O} = \ln\left(\frac{R_{\text{sample}}}{R_{\text{standard}}}\right) \quad (3)$$

The natural log transformation used in the delta-prime notation, as compared to traditional delta notation, is required because at the level of precision used to calculate  $\Delta^{17}\text{O}$  values, the non-linearity of three-isotope mass dependent fractionation is an important consideration (e.g., Miller 2002; Luz and Barkan, 2010; Aron et al., 2021). The slope of the preferred reference line,  $\lambda_{\text{ref}}$ , is commonly taken as the trend of the global meteoric water line (GMWL), 0.528, and we follow this convention (Luz and Barkan, 2010; Sharp et al., 2018; Aron et al., 2021; Sharp and Wostbrock, 2021). Variability in  $\Delta^{17}\text{O}$  is much smaller than that of  $\delta^{18}\text{O}$ , so we multiply values by  $10^6$  for convenience (per meg notation, where 1 per meg = 0.001‰). Within this framework, the three-isotope fractionation exponent ( $\theta$ ) relates the fractionation factors for the system as (Mook, 2000):

$$\theta_{a-b} = \frac{\ln(^{17/16}\alpha_{a-b})}{\ln(^{18/16}\alpha_{a-b})} \quad (4)$$

where  $\alpha_{a-b}$  is the fractionation factor between two phases exchanging isotopes (i.e.,  $R_a/R_b$ ). The values of  $\lambda$  and  $\theta$  are mathematically equivalent, but we reserve  $\theta$  for simple processes like isotope fractionation between two phases and  $\lambda$  for a regression through a dataset that results from multiple processes.

Triple oxygen isotope data are valuable because they directly inform the interpretation of widely employed  $\delta^{18}\text{O}$  records. The information added by considering

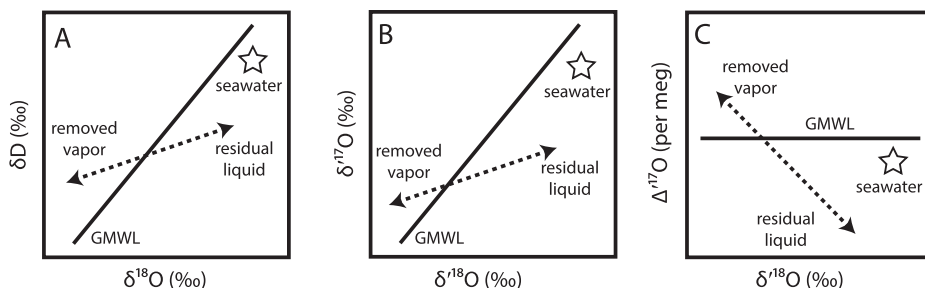


Fig. 1. Schematic diagrams showing relationships among  $\delta D$ ,  $\delta^{17}\text{O}$ ,  $\delta^{18}\text{O}$ , and  $\Delta^{17}\text{O}$  during evaporation. (a) In  $\delta D$  vs.  $\delta^{18}\text{O}$  space, a water initially on the Global Meteoric Water Line (GMWL; slope  $\approx 8$ ) evolves away from it during evaporation and *d-excess* becomes more negative. (b) In  $\delta^{17}\text{O}$  vs.  $\delta^{18}\text{O}$  space (triple oxygen isotope space), a water initially on the GMWL (slope  $\approx 0.528$ ) evolves away from it during evaporation. (c) The same scenario in (b) represented in  $\Delta^{17}\text{O}$  vs.  $\delta^{18}\text{O}$  space. Evaporation leads to water with lower  $\Delta^{17}\text{O}$  than the parent water.

$\Delta^{17}\text{O}$  data (via  $\delta^{17}\text{O}$  and  $\delta^{18}\text{O}$  data) is analogous to how combining  $\delta D$  and  $\delta^{18}\text{O}$  allows for more detailed inquiry, via the *d-excess* parameter ( $d\text{-excess} = \delta D - 8 \times \delta^{18}\text{O}$ ), than with one isotope system alone (Fig. 1) (e.g., Dansgaard, 1964; Frölich et al., 2002; Landais et al., 2010; Welker, 2012; Pfahl and Sodemann, 2014; Schoenemann and Steig, 2016; Zongxing et al., 2016; Dütsch et al., 2017; Ampuero et al., 2020; Bershaw et al., 2020; Aron et al., 2021). This is particularly useful for minerals, like carbonates, that preserve information about ancient hydrologic processes but do not contain hydrogen isotopes needed to calculate *d-excess* (although see, e.g., Affolter et al., 2015). Additionally, theoretical calculations, laboratory experiments, and natural experiments suggest that  $\theta$  is weakly temperature-sensitive and  $\Delta^{17}\text{O}$  has different responses to hydrologic change than  $\delta^{18}\text{O}$  (resulting from, e.g., evaporation, Rayleigh distillation, and calcite formation kinetic effects; Criss, 1999; Barkan and Luz, 2007; Cao and Liu, 2011; Surma et al., 2015; Gásquez et al., 2017, 2018; Hayles et al., 2018; Guo and Zhou, 2019a; Guo and Zhou, 2019b; Passey and Ji, 2019; Wostbrock et al., 2020a; Schuble and Young, 2021; Voigt et al., 2021). With relevance to near-surface modern climatology and paleoclimatology, measurements and models of  $\Delta^{17}\text{O}$  in water (liquid, vapor, and ice), carbonates, biological apatites, and gypsum have been used to model or infer, for example, variations in relative humidity, evaporation intensity, atmospheric patterns, and paleotopography (Landais et al., 2008; Landais et al., 2010; Risi et al., 2010; Risi et al., 2013; Passey et al., 2014; Li et al., 2015; Gásquez et al., 2018; Passey and Ji, 2019; Uechi and Uemura, 2019; Gásquez et al., 2020; Aron et al., 2021; Ibarra et al., 2021). Thus, combining  $\Delta^{17}\text{O}$  data with traditional  $\delta^{18}\text{O}$  data allows for better constrained paleoclimate interpretations than previously possible.

Modern meteoric water  $\Delta^{17}\text{O}$  is thought to be largely controlled by effects like the evaporation conditions at the moisture source region (e.g., relative humidity and turbulence), local evaporation, moisture recycling, and mixing (Luz and Barkan, 2010; Risi et al., 2010; Risi et al., 2013; Li et al., 2015; Uechi and Uemura, 2019; Aron et al., 2021). Previous characterizations of cave system  $\Delta^{17}\text{O}$  have therefore focused on connecting  $\Delta^{17}\text{O}$  in cave materials to that of precipitation and to climate variables. For example,

in a study of meteoric waters at Milandre Cave in Switzerland, Affolter et al. (2015) noted the similarity of  $\Delta^{17}\text{O}$  values from precipitation, drip waters, and fluid inclusions within speleothems. Gásquez et al. (2017, 2020) explored  $\Delta^{17}\text{O}$  in meteoric waters, gypsum hydration waters, and reconstructed parent waters in several caves in the gypsum karst of the Sorbas Basin, Spain. From these values, they discerned that gypsum formation waters are a mixture of condensation and infiltration water, consistent with gypsum formation under variable conditions of winter atmospheric relative humidity. Sha et al. (2020) studied cave drip waters, modern speleothems, and ancient speleothems. From paired  $\Delta^{17}\text{O}$  analyses of drip water and modern speleothems, they derived empirical fractionation factors for the carbonate-water reaction. They used this calibration to reconstruct formation water  $\Delta^{17}\text{O}$  for pairs of speleothem samples and model how regional relative humidity changed (Barkan and Luz, 2007) across major climate transitions like the Last Glacial Maximum (25–20 ka; ka = thousands of years before present) to the Holocene (<11.7 ka).

Theoretical work has also provided a basis for predicting how  $\Delta^{17}\text{O}$  is influenced by mineral growth processes (no related empirical investigations exist to our knowledge). Modeled kinetic effects between water and carbonate during calcite formation will increase  $\delta^{18}\text{O}_{\text{calcite}}$  and  $\Delta^{17}\text{O}_{\text{calcite}}$  (Guo and Zhou, 2019a; Guo and Zhou, 2019b). In this model, within-cave effects (e.g.,  $\text{CO}_2$  degassing at the drip site) and prior calcite precipitation drive the same positive co-variation signal, so we group them together as “cave kinetic effects.” Note that while cave kinetic effects also potentially include evaporation within the cave, this is an unlikely scenario for most samples which have been preferentially collected deep in cave systems where relative humidity commonly approaches 100 % (Lachnit, 2009; but see also Gásquez et al. 2017, 2020).

## 1.2. Exploring a geochemical framework for triple oxygen isotopes in speleothems

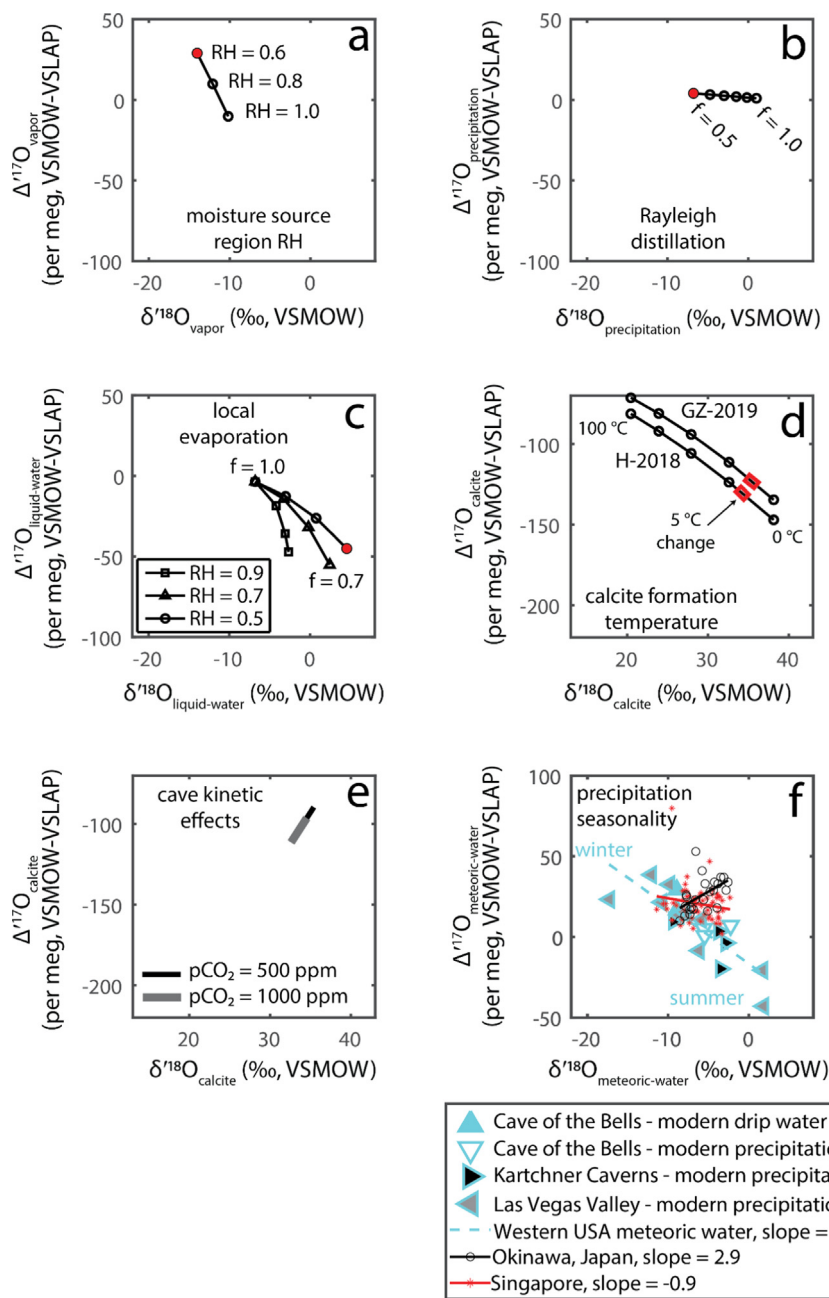
The existing body of work points towards a geochemical framework that may be used to identify the primary driver(s) of speleothem triple oxygen isotope composition (Figs. 2 and 3). For example, when data are viewed in  $\Delta^{17}\text{O}$  vs.

$\Delta^{18}\text{O}$  space, positive trends should theoretically be produced by cave kinetic effects (+7 per meg/‰, or a  $\delta^{17}\text{O}$  vs.  $\delta^{18}\text{O}$  slope of  $\approx 0.535$ ; Guo and Zhou, 2019a; Guo and Zhou, 2019b). Slightly negative to near-horizontal trends (between  $-1$  to  $0$  per meg/‰ over  $-25$  to  $35$  °C, or  $\delta^{17}\text{O}$  vs.  $\delta^{18}\text{O}$  slopes of  $0.527$ – $0.528$ ) are produced by isotope fractionation resulting from Rayleigh distillation processes (e.g., rainout amount) (Horita and Wesolowski, 1994; Criss, 1999; Barkan and Luz, 2005; Aron et al., 2021).

More negative trends ( $<-1$  per meg/‰) may be produced by changes in carbonate formation temperature and evaporation conditions. Carbonate formation temperature effects are expected to produce  $\Delta^{17}\text{O}$  vs.  $\delta^{18}\text{O}$  trends of approximately  $-3$  to  $-2$  per meg/‰ over  $0$ – $25$  °C

( $\Delta^{17}\text{O}$  vs.  $\delta^{18}\text{O}$  slopes of  $\approx 0.525$ – $0.526$ ) (Cao and Liu, 2011; Hayles et al., 2018; Guo and Zhou, 2019b; Wostbrock et al., 2020a; Schauble and Young, 2021). Mineralization temperature sensitivity for  $\Delta^{17}\text{O}$  is therefore on the order of  $<0.7$  per meg/°C (Cao and Liu, 2011; Passey et al., 2014; Hayles et al., 2018; Guo and Zhou, 2019b; Wostbrock et al., 2020a; Schauble and Young, 2021).

Evaporation of waters, another process capable of producing negative trends, has been conceptually modeled using two primary types of isotopic fractionation (Criss, 1999); (1) equilibrium fractionation into a thin, saturated boundary layer (following a  $\delta^{17}\text{O}$  vs.  $\delta^{18}\text{O}$  slope of  $0.529$ ; Barkan and Luz, 2005), and (2) kinetic fractionation



as water vapor diffuses away from the water surface ( $\delta^{17}\text{O}$  vs.  $\delta^{18}\text{O}$  slope of 0.5185; Barkan and Luz, 2007) (Luz and Barkan, 2010; Surma et al., 2015; Surma et al., 2018; Passey and Ji, 2019). As a result of kinetic fractionation, data from evaporating waters show negative trends (<−2 per meg/‰; Barkan and Luz, 2007; Luz and Barkan, 2010; Surma et al., 2015; Gázquez et al., 2018; Passey and Ji, 2019; Voigt et al., 2021).

In the context of this study, evaporation can refer to relative humidity at the moisture source or to local evaporation during precipitation events (e.g., sub-cloud evaporation) and infiltration (e.g., soil evaporation). Local and far-field aridity effects may be differentiated based on temporal changes and other proxy information. For example, increasingly arid conditions at the moisture source increase  $\Delta^{17}\text{O}$  while increasingly arid local conditions decrease  $\Delta^{17}\text{O}$  (Fig. 2a and c) (e.g., Surma et al., 2015; Uechi and Uemura, 2019). Note that previous studies have clearly identified trends in evaporated waters that are significantly lower than −2 per meg/‰ (Criss, 1999; Surma et al., 2015; Gázquez et al., 2018; Passey and Ji, 2019). These trends can be measurably nonlinear after significant evaporation has occurred (>5%), but the  $\delta^{18}\text{O}$  range required probably precludes application to most published speleothem records.

The observed precipitation seasonality at a site may be driven by more than one process and resulting trends in  $\Delta^{17}\text{O}$  vs.  $\delta^{18}\text{O}$  space can vary from positive to negative (Fig. 2f). For example, in Okinawa, Japan, Uechi and Uemura (2019) used precipitation triple oxygen isotope composition to successfully reconstruct source region relative humidity, as inferred from air mass backward trajectories. This result necessitates evaporation as a strong control on precipitation isotope composition (i.e., moisture source region conditions), which should lead to a negative trend in  $\Delta^{17}\text{O}$  vs.  $\delta^{18}\text{O}$  space. However, their data counter-intuitively exhibits a positive trend. This pattern may occur because intense Rayleigh distillation in summer decreases

$\delta^{18}\text{O}$  with minimal change in  $\Delta^{17}\text{O}$ , effectively reversing the trend expected from evaporation alone (Fig. 2b, 2f) (Uemura et al., 2012). However, this mechanistic explanation may not be applicable everywhere and other trends have been observed in monsoonal climates. In Singapore, He et al. (2021) found no relationship between precipitation  $\delta^{18}\text{O}$  and  $\Delta^{17}\text{O}$  and were not able to reconstruct source region relative humidity. Regardless of the processes controlling precipitation triple oxygen isotope composition, modern datasets will be helpful in defining  $\Delta^{17}\text{O}$  vs.  $\delta^{18}\text{O}$  trends at sites of paleoclimate interest, where speleothem records have provided important insights for climate dynamics and forcing.

In this study, we explore how the above geochemical framework for triple oxygen isotopes (Fig. 3) might be used to identify primary drivers of variation in speleothem oxygen isotope composition and provide a better constraint on paleoclimate reconstructions than via  $\delta^{18}\text{O}$  alone. Each process has variability in its associated trend and in detail none are truly linear. Given current analytical precision for  $\Delta^{17}\text{O}$  analyses, we use slopes of +7, −1 to 0, and <−2 per meg/‰ (0.535, 0.528, and <0.526 in  $\Delta^{17}\text{O}$  vs.  $\delta^{18}\text{O}$  space, respectively) as representative approximations for cave kinetic, Rayleigh distillation, and evaporation/mineralization temperature/seasonality processes (Fig. 3).

We recognize that complicated, multi-process scenarios exist. However, consider the utility of triple oxygen isotope data in a situation where data have a  $\Delta^{17}\text{O}$  vs.  $\delta^{18}\text{O}$  trend of 0 per meg/‰ and interpretation may be ambiguous. Assuming the data trend was created by a mix of evaporation (−3 per meg/‰) and cave kinetic (+7 per meg/‰) processes, climate (evaporation) would still drive an overwhelming 70 % of the signal [i.e.,  $0.7*(-3) + 0.3*(7) = 0$ ]. If data were also a function of Rayleigh distillation, or if data defined a negative trend, interpretations of climate-related drivers would only be strengthened. In addition, note that many speleothem records are interpreted in the context of one or two dominant climate processes, even

Fig. 2. Overview of processes relevant to speleothem triple oxygen isotopes in  $\Delta^{17}\text{O}$  vs.  $\delta^{18}\text{O}$  space. (a)–(e) follow how triple oxygen isotopes fractionate in a hypothetical sample from its moisture source to final deposition in a speleothem. Lines are used to highlight trends, but only in panels (b), (c), and (e) do they represent temporal paths of isotope evolution. In (a)–(c), the red dot identifies the water composition used for the next panel. Modeled calcites in (d) and (e) are both derived from the identified water composition in (c). Note that axes all have the same relative scale ranges, but those of (d) and (e) are shifted to account for water-calcite fractionation. (a) The vapor evaporated from a moisture source (VSMOW) under different relative humidity conditions (RH = relative humidity, temperature = 15 °C). (b) Precipitation isotope composition during transport as a function of Rayleigh-style rainout (f = fraction of water remaining with 10% intervals, temperature = 5 °C). (c) Water isotope composition during pan-evaporation at the cave site (e.g., during precipitation or infiltration) under different relative humidity conditions (f = fraction of water remaining, temperature = 15 °C). (d) Speleothem isotope composition for equilibrium formation at different temperatures (25 °C intervals) calculated using two different theoretical models for  $\theta_{\text{CaCO}_3-\text{H}_2\text{O}}$  (H-2018 after Hayles et al., 2018; GZ-2019 after Guo and Zhou, 2019b). Red boxes highlight the effect of a 5 °C change (e) Trend of cave kinetic processes (prior calcite precipitation, fast degassing) on speleothem isotope composition at 25 °C (after Guo and Zhou, 2019a, 2019b). Thin black and thick gray lines represent cave pCO<sub>2</sub> conditions of 500 and 1000 ppm, respectively. (f) Meteoric water data from the western USA (cyan triangles; this study), Okinawa, Japan (black circles; Uechi and Uemura, 2019), and Singapore (red stars; He et al., 2021) as examples of potential seasonal variability in precipitation isotope composition (see also Fig. 7). The “winter” and “summer” labels refer to western USA waters; winter samples tend to have more negative  $\delta^{18}\text{O}$  and positive  $\Delta^{17}\text{O}$  than summer waters (and vice versa for summer samples). For western USA meteoric waters, Cave of the Bells drip waters are upward-pointing triangles with cyan fill, Cave of the Bells precipitation samples are downward-pointing triangles with white fill, Kartchner Caverns precipitation samples are right-pointing triangles with black fill, and Nevada precipitation samples are left-pointing triangles with gray fill. The ordinary least squares regression for all western USA meteoric waters from this study is the dashed cyan line, for Okinawa data is the black solid line, and for Singapore data is the red solid line. (For interpretation of the references to colour in this figure legend, the reader is referred to the web version of this article.)

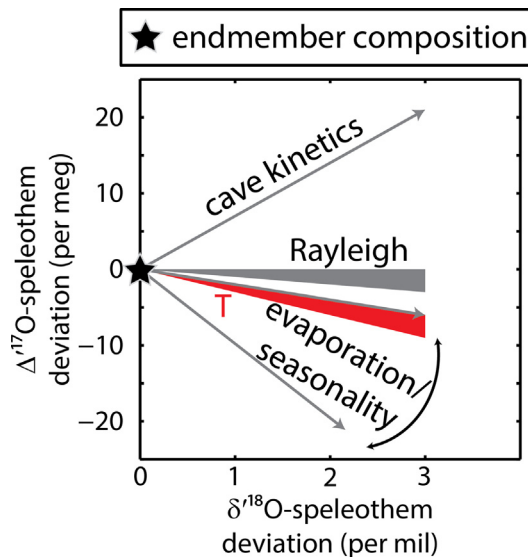


Fig. 3. Summary of triple oxygen isotope drivers relevant to speleothem triple oxygen isotopes in  $\Delta^{17}\text{O}$  vs.  $\delta^{18}\text{O}$  space. Processes influence a hypothetical endmember isotope composition (black star). The cave kinetics, Rayleigh (gray wedge), mineralization temperature (T, red wedge) and evaporation/seasonality trends have characteristic slopes of +7, -1 to 0, -3 to -2, and  $\leq -2$  per meg‰, respectively ( $\Delta^{17}\text{O}$  vs.  $\delta^{18}\text{O}$  slopes of 0.535, 0.527–0.528, 0.525–0.526, and  $\leq 0.526$ , respectively). The mineralization temperature trend is plotted separately from the evaporation/seasonality trend here to emphasize its magnitude for a given temperature change. It is shown for a  $\approx 12\text{ }^{\circ}\text{C}$  change (a  $\approx 3\text{‰}$   $\delta^{18}\text{O}$  change; e.g., Kim and O’Neil, 1997), but its potential influence will be determined by expected temperature variability. Note the negative precipitation seasonality trend is site specific for this study and represents a summation of hydrologic processes (Figs. 2f and 7). The evaporation trend can vary widely because it is dependent on relative humidity, magnitude of distillation, and diffusion (see also Section 1.2 Exploring a geochemical framework for triple oxygen isotopes in speleothems).

if the specific processes are debated (Wang et al., 2001; Maher and Thompson, 2012; Lachniet et al., 2014; Steponaitis et al., 2015; Wang et al., 2017). If these interpretations are justified, simple geochemical models (Fig. 2) should adequately explain the first-order variability in  $\Delta^{17}\text{O}$  vs.  $\delta^{18}\text{O}$  data. To this end, we explore triple oxygen isotopes in modern meteoric waters and late Quaternary speleothems from three cave systems in the western USA. Each  $\delta^{18}\text{O}_{\text{speleothem}}$  record has a paleoclimate interpretation based on a few dominant processes suitable for testing. We first review prior work and interpretations of  $\delta^{18}\text{O}_{\text{speleothem}}$  before describing our experimental setup and methodology. We then present the results, use the framework to make paleoclimate inferences at our study site and other locations, and conclude with an outlook for using triple oxygen isotopes in speleothem-based paleoclimate reconstructions.

## 2. STUDY SITES AND SPELEOTHEM RECORD OVERVIEWS

We investigated speleothems from Cave of the Bells (AZ), Leviathan Cave (NV), and Lehman Caves (NV) as well as

archived and new meteoric waters (rain, snow, and drip water) from Arizona and Nevada (Wagner et al., 2010; Lachniet et al., 2014; Lachniet et al., 2020) (Fig. 4a). All caves are in the southwestern USA, with Leviathan and Lehman Caves located approximately 180 km apart. Age models and  $\delta^{18}\text{O}_{\text{speleothem}}$  records have previously been published from all three caves so we briefly summarize the basic paleoclimate interpretations of these records. In addition, we present a new speleothem record from Lehman Caves (LMC-12b) that was selected for this study because it exhibits extremely large  $\delta^{18}\text{O}$  variability ( $\approx 7\text{‰}$  VPDB) from 16–6 ka that was inconsistent with (near) equilibrium formation conditions. Recognizing that LMC-12b likely represents a kinetically influenced sample, we present the  $\delta^{18}\text{O}_{\text{speleothem}}$  record in this section analogous to the overviews provided for the Cave of the Bells and Leviathan Cave records (see Supplementary Material text for methods and the age model; Supplementary Material, Tables S4 and S5, Figs. S3 and S4).

### 2.1. Paleoclimate reconstructions of Cave of the Bells and Leviathan Cave

#### 2.1.1. The Cave of the Bells record (COB-01-02)

The Cave of the Bells record spans approximately 53–8 ka (Fig. 4b) (Wagner et al., 2010). The  $\delta^{18}\text{O}_{\text{speleothem}}$  data vary from  $-11.4$  to  $-7.8\text{‰}$  VPDB (3.5‰ total range) and have clear connections to regional- and global-scale climate change in the form of, for example, the timing of interstadial stages inferred from polar ice core records (Svensson et al., 2008). The  $\delta^{18}\text{O}_{\text{speleothem}}$  record was not interpreted in the context of kinetic effects because sample COB-01-02 was collected deep within Cave of the Bells, where relative humidity approaches 100 %, and the data set passed a modified “Hendy test” (Hendy, 1971) that did not find time-transgressive covariation of  $\delta^{18}\text{O}$  and  $\delta^{13}\text{C}$  values. Instead, the data were interpreted in the context of modern climate and cave conditions where summer rain is related to the North American Monsoon (50–65 % of mean annual precipitation) and winter precipitation is associated with westerly storms (Adams and Comrie, 1997; Higgins et al., 1997; Wagner et al., 2010). Modern  $\delta^{18}\text{O}_{\text{rainfall}}$  data show large seasonal changes but  $\delta^{18}\text{O}_{\text{drip-water}}$  values are biased towards winter rainfall values ( $\approx -9\text{‰}$  VSMOW), suggesting that a substantial percentage of modern summer rainfall is lost to evapotranspiration and runoff before it can infiltrate. Based on these observations and a precipitation isotope data set spanning 1984–2004, Wagner et al. (2010) interpreted  $\delta^{18}\text{O}_{\text{speleothem}}$  in terms of a winter amount effect, or winter aridity, where more negative  $\delta^{18}\text{O}_{\text{speleothem}}$  values corresponded to wetter winters. They also noted that formation temperature could affect  $\delta^{18}\text{O}_{\text{speleothem}}$  values (e.g., Kim and O’Neil, 1997), but largely attributed the signal to changing precipitation amounts.

Eastoe and Dettman (2016) suggested alternate explanations, based on a 32-yr (1981–2012)  $\delta^{18}\text{O}_{\text{precipitation}}$  record from nearby Tucson, AZ (60 km distant) with weaker or non-significant correlations between precipitation amount and  $\delta^{18}\text{O}$  over seasonal to decadal timescales. These authors proposed that changes in the ratio of summer to winter precipitation, moisture source region, or the fre-

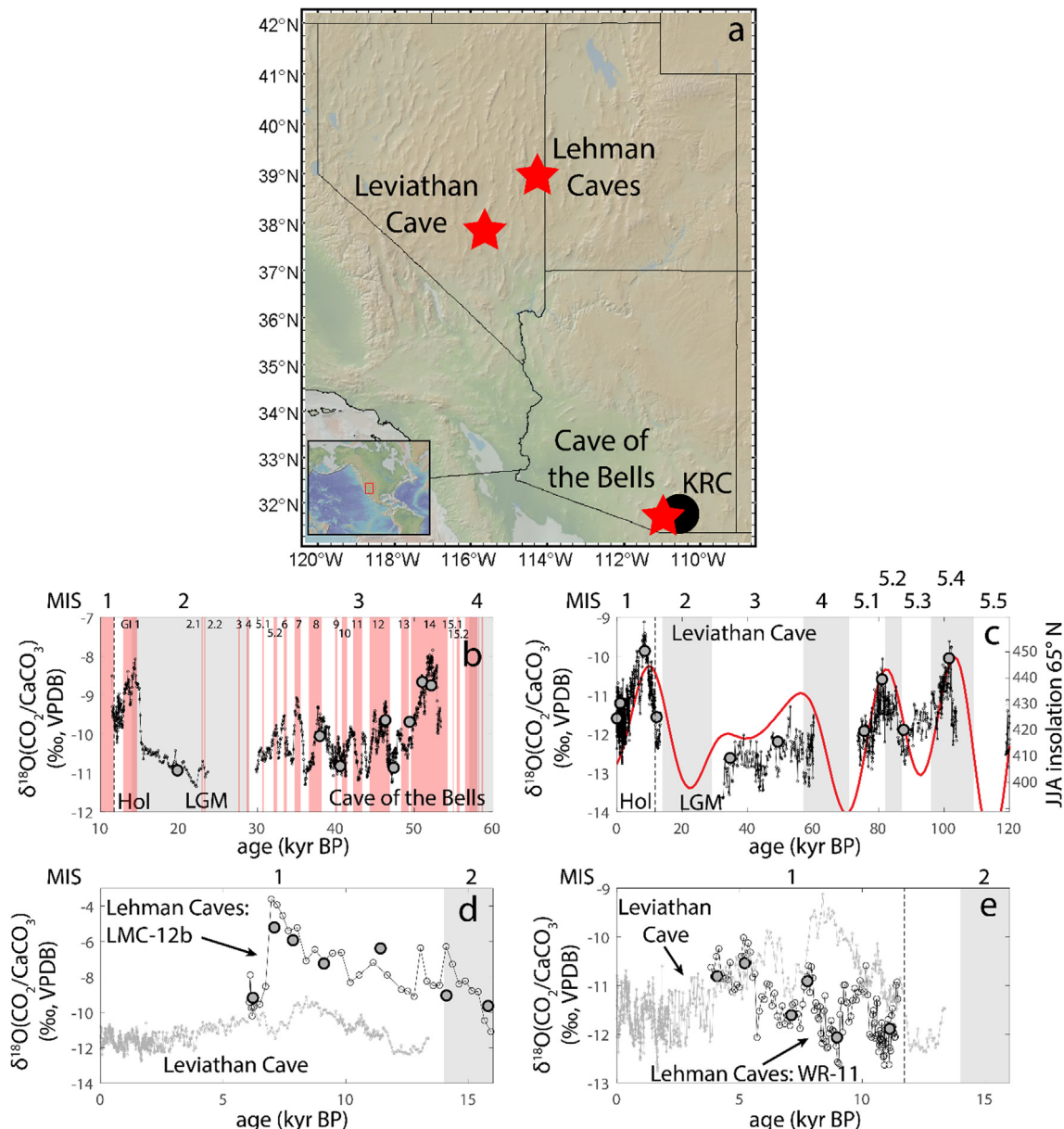


Fig. 4. Location study sites and their  $\delta^{18}\text{O}_{\text{speleothem}}$  records. (a) Map of the southwestern USA showing cave locations (red stars) as well as Kartchner Caverns (black circle), where we only sampled for meteoric water. Figure made with GeoMapApp (<http://www.geomapapp.org/>; Ryan et al., 2009). (b)–(e) Previously published  $\delta^{18}\text{O}_{\text{speleothem}}$  records overlain with this study's data (gray circles). The “ $\delta^{18}\text{O}(\text{CO}_2/\text{CaCO}_3)$ ” notation on the y-axes identifies data as  $\delta^{18}\text{O}$  analyses of  $\text{CaCO}_3$  made on evolved  $\text{CO}_2$  (see also Section 4.1 Materials and nomenclature). Note different axes ranges, which we scale to individual records to emphasize our sampling of the available  $\delta^{18}\text{O}$  range as well as overall patterns in the records, and that data are presented relative to VPDB as in the original publications. Panels show (b) Cave of the Bells (COB-01-02) with Greenland Interstadials (GI) numbered (light pink bands; Rasmussen et al., 2014), (c) Leviathan Cave (LC-1) with JJA insolation at 65°N (red line; Berger and Loutre, 1991), and (d and e) Lehman Caves records LMC-12b and WR-11, respectively (Wagner et al., 2010; Lachniet et al., 2014; Steponaitis et al., 2015; Lachniet et al., 2020). The Lehman Caves  $\delta^{18}\text{O}$  records are interpreted to be affected by local kinetic processes (see Section 2 Study sites and speleothem record overviews) and the Leviathan Cave record is also plotted for comparison (gray line). Typical error bars for data are smaller than symbols and not shown for clarity. Marine Isotope Stages (MIS, gray and white bands) are labeled above each panel (LR04 benthic stack; Lisiecki and Raymo, 2005), the approximate time of the Last Glacial Maximum is marked at 20–25 ka (LGM), and the start of the Holocene (Hol) is marked at 11.7 ka (dashed line).

quency of extreme precipitation events may also explain the Cave of the Bells  $\delta^{18}\text{O}_{\text{speleothem}}$  data. However, all published interpretations of the Cave of the Bells record are predi-

cated on the idea that the  $\delta^{18}\text{O}_{\text{speleothem}}$  record was not significantly influenced by local evaporation or cave kinetic effects.

### 2.1.2. The Leviathan Cave record (LC-1)

Leviathan Cave sample LC-1 is from the Great Basin and covers much of the last glacial-interglacial cycle, including 103–74, 60–33, and 13–0 ka (Lachniet et al., 2014; Lachniet et al., 2017; Lachniet et al., 2020) (Fig. 4c). The  $\delta^{18}\text{O}$  time series varies from  $-13.6$  to  $-9.1\text{\textperthousand}$  VPDB (4.5% total range). This sample is part of the “Leviathan Chronology,” which combines samples from two other Nevada Caves, Pinnacle Cave and Lehman Caves, to show a Great Basin-wide response to regional- and global-scale climate change via precessional-scale orbital forcing (Lachniet et al., 2014; Lachniet et al., 2017; Lachniet et al., 2020). The Leviathan Cave record was not interpreted in the context of kinetic effects because the modern cave environment is characterized by constant temperature and relative humidity approaches 100 %. In Nevada, modern  $\delta^{18}\text{O}_{\text{precipitation}}$  values are strongly correlated with temperature, both on temporal and spatial (i.e. across the state) scales, and are inversely correlated with the latitude of the moisture source (Lachniet et al., 2020). Therefore, the authors interpreted  $\delta^{18}\text{O}_{\text{speleothem}}$  as a proxy for the temperature and moisture source region of winter precipitation.

## 2.2. The Lehman Caves records (LMC-12b and WR-11)

### 2.2.1. Sample LMC-12b age model, $\delta^{18}\text{O}_{\text{speleothem}}$ record construction, and $\delta^{18}\text{O}$ -based interpretation

We collected Lehman Caves sample LMC-12b as a broken and down stalagmite in 1999 and present a preliminary record from U-series and  $\delta^{18}\text{O}$  analyses (Supplementary Material, Figs. S3 and S4, Tables S4 and S5). While the sample grew intermittently in three periods over the last 120 ka (123–120, 53–43, and 16–6 ka), for this study we present the  $< 16$  ka section to compare with the nearby, similar-aged section of the Leviathan Cave record. Within this section, the  $\delta^{18}\text{O}_{\text{speleothem}}$  record ranges from  $-11.1$  to  $-3.6\text{\textperthousand}$  VPDB (7.5% total range) and mimics the shape of the Leviathan Cave record (Fig. 4d). This suggests that, at least in part, the Lehman Caves  $\delta^{18}\text{O}_{\text{speleothem}}$  record was created by similar  $\delta^{18}\text{O}_{\text{precipitation}}$  variability invoked to explain the Leviathan Cave record. However, given its much larger range over the same time period ( $\approx 7\text{\textperthousand}$  vs.  $3.5\text{\textperthousand}$ , respectively) and that  $\delta^{18}\text{O}_{\text{speleothem}}$  is significantly higher than would be expected from carbonate formed in equilibrium with modern cave water ( $\approx -13.5$  to  $-11.5\text{\textperthousand}$  VPDB; Coplen, 2007; Kim and O’Neil, 1997; Lachniet et al., 2014; Wostbrock et al., 2020a; Friedman and O’Neil, 1977; Affek and Zaarur, 2014), we consider it likely that sample LMC-12b was additionally influenced by evaporative and/or cave kinetic effects.

### 2.2.2. Sample WR-11

Lehman Caves speleothem WR-11 was sampled for stable isotope- ( $\delta^{18}\text{O}$  and  $\delta^{13}\text{C}$ ) and elemental ratio- (e.g., Mg/Ca) based paleoclimate records (Steponaitis et al., 2015). The record covers much of the Holocene, including 11.5–3.8 ka (Fig. 4e), with  $\delta^{18}\text{O}$  varying from  $-12.6$  to  $-10.0\text{\textperthousand}$  VPDB (2.6% total range).

Because relative humidity in the modern cave is high and modern cave waters fall on the local meteoric water line, the record is unlikely to have experienced significant within-cave evaporation. However, the  $\delta^{18}\text{O}_{\text{speleothem}}$  record does not replicate with another record from the same cave (CDR3; Steponaitis et al., 2015) and shows only partial agreement with the nearby Leviathan Cave Record (LC-1) (Lachniet et al., 2014) that is strongly correlated to orbital insolation values over the last glacial cycle (Fig. 4c). In addition, the  $\delta^{18}\text{O}$  record correlates with the  $\delta^{13}\text{C}$  and Mg/Ca records, which show overall increases through the Holocene ( $-5$  to  $-2\text{\textperthousand}$  VPDB and 2 to 6 mmol/mol, respectively). The authors therefore suggested that, in addition to changes in  $\delta^{18}\text{O}_{\text{precipitation}}$ , variable cave kinetic effects may have been important in driving  $\delta^{18}\text{O}_{\text{speleothem}}$ . This could have been caused by prior calcite precipitation, where slower infiltration rates permitted substantial CO<sub>2</sub> degassing, and therefore calcite precipitation, before water reached the drip site. Alternatively, kinetic fractionation may have occurred at the drip site from rapid CO<sub>2</sub> degassing forcing calcite precipitation.

## 3. EXPERIMENTAL SETUP AND PREDICTED TRENDS

### 3.1. Experimental setup

#### 3.1.1. Analytical considerations

Our methodology for measuring triple oxygen isotopes in waters and carbonates (see below, section 4.4 *Triple oxygen isotope analyses*) allowed for  $\Delta^{17}\text{O}$  analyses with single-replicate external precision of  $\approx 10$  per meg ( $1\sigma$ ), similar to that achieved by other laboratories and methodologies (Barkan and Luz, 2007; Passey et al., 2014; Gázquez et al., 2018; Sha et al., 2020; Wostbrock et al., 2020a, 2020b; Passey and Levin, 2021). We considered this precision and the long analytical time ( $\approx 2.5$  hr/replicate) as part of our experimental setup. Because  $\Delta^{17}\text{O}$  values are expected to vary by only a few tens of per meg, robustly defining a  $\Delta^{17}\text{O}$  excursion requires many replicates or samples with a large  $\delta^{18}\text{O}$  range (i.e., maximizing the  $\delta^{18}\text{O}$  variability maximizes the potential to detect  $\Delta^{17}\text{O}$  variability). We used a Monte Carlo assessment of our analytical capabilities to identify the likely number of samples and replicates that would reasonably identify data trends ( $> 90$  % of the time) (Supplementary Material text and Fig. S1). For speleothems exhibiting 2.5–4.5%  $\delta^{18}\text{O}$  variability (COB-01–02, LC-1, and WR-11), the results suggested that 5–10 samples with 4 replicates each would be required to distinguish Rayleigh distillation and cave kinetic trends (modeled as trends with slopes of 0 and  $+ 7$  per meg/ $\text{\textperthousand}$ , respectively). On the other hand, discerning Rayleigh distillation and evaporation trends is more difficult because the slopes can be more similar (0 and  $\leq -2$  per meg/ $\text{\textperthousand}$ , respectively). Even for a speleothem exhibiting  $\approx 7\text{\textperthousand}$   $\delta^{18}\text{O}$  variability (LMC-12b), the results suggested that 17 samples with 4 replicates might be required to distinguish Rayleigh-style and evaporation trends. We therefore maximized our ability to resolve  $\Delta^{17}\text{O}$  signals by (1) drilling samples to maximize

the  $\delta^{18}\text{O}_{\text{speleothem}}$  range investigated, (2) making only qualitative predictions of  $\Delta^{17}\text{O}$  vs.  $\delta^{18}\text{O}$  trends (positive, negative, or horizontal), (3) and combining data sets where feasible to increase the  $\delta^{18}\text{O}_{\text{speleothem}}$  range investigated.

### 3.1.2. Predicted trends

The Cave of the Bells and Leviathan Cave records share attributes with other published speleothem records that are accepted by the paleoclimate community as useful for paleoclimate reconstruction. The records (1) have supporting evidence that they were minimally influenced by cave kinetic effects (e.g., via cave sampling strategy and Hendy tests; [Hendy, 1971](#)), (2) show unambiguous ties to established paleoclimate phenomena (e.g., correlation to other regional and global paleoclimate records), (3) are interpreted based on an understanding of the modern hydrologic system, and (4) have interpretive frameworks that are limited to a few major processes. In contrast, although the Lehman Caves samples were chosen based on similar parameters (e.g., they were taken from deep within the cave), they were likely influenced by cave kinetic or local evaporation effects (i.e., the LMC-12b  $\delta^{18}\text{O}$  profile mimics that of LC-1 but is greatly exaggerated; the WR-11  $\delta^{18}\text{O}$  record does not replicate nearby  $\delta^{18}\text{O}$  records and covaries with the  $\delta^{13}\text{C}$  and Mg/Ca records).

If the previously published interpretive frameworks developed for each of the  $\delta^{18}\text{O}_{\text{speleothem}}$  records are correct and  $\delta^{18}\text{O}$  variability largely results from one or two major processes, then variability in the  $\Delta^{17}\text{O}$  vs.  $\delta^{18}\text{O}$  data should be well described by the associated geochemical models of [Fig. 2](#). This parsimonious approach inherently assumes that the dominant processes controlling  $\delta^{18}\text{O}_{\text{speleothem}}$  did not change through time, which could be tested in future studies by examining individual climate intervals with higher-resolution sampling. If previous interpretations are viable, data from Cave of the Bells and Leviathan Cave should show near-horizontal to negative trends consistent with control by Rayleigh distillation, temperature of mineralization, precipitation seasonality, and moisture source conditions. Additionally, control by regional-scale processes means that the reconstructed formation waters (especially for Holocene samples with well-constrained formation temperatures) should fall on the associated modern meteoric water line.

In contrast, if the Lehman Caves stalagmites selected for study were significantly influenced by cave-specific kinetic processes, data should not create horizontal trends. Sample LMC-12b should exhibit either a negative or positive trend in response to variable local evaporation or cave kinetic effects while data from sample WR-11 should display a positive trend consistent with variable cave kinetic effects. In addition, because the Leviathan Cave and Lehman Caves systems are nearby, it is reasonable to expect they experienced the same regional climate change through time. In conjunction with how Lehman Caves sample LMC-12b presents an exaggerated profile of Leviathan Cave stalagmite LC-1, this additionally suggests that a combined data set should emphasize the trend observed in the LMC-12b data set, regardless of individual data set trends.

## 4. METHODOLOGY

### 4.1. Materials and nomenclature

The data presented here comprise  $\delta^{18}\text{O}$  and  $\Delta^{17}\text{O}$  analyses from speleothem carbonates and meteoric waters. Published triple oxygen isotope analyses of most materials are temporally and spatially limited, so we used isotopic analyses of water samples to understand seasonal variability in precipitation and drip waters (as in [Fig. 2f](#)). We tested our predictions using isotopic analyses of speleothem carbonates and modern waters in conjunction with reconstructed formation water isotope composition. We used several different methodologies to acquire  $\delta^{18}\text{O}$  data because “traditional”  $\delta^{18}\text{O}$  methods [cavity ringdown spectroscopy (CRDS) and phosphoric acid digestion–CO<sub>2</sub> Isotope Ratio Mass Spectrometry for waters and carbonates, respectively] have better precision than our reduction-fluorination triple oxygen isotope methodology (generic 1  $\sigma$  values of < 0.2‰ and 0.8‰, respectively) due to fractionations occurring during sample preparation. However, these fractionations do not materially alter the high-precision  $\Delta^{17}\text{O}$  analyses because they affect samples in a mass-dependent way ([Barkan and Luz, 2007](#); [Schoenemann et al., 2013](#); [Passey et al., 2014](#); [Wostbrook et al. 2020b](#)). We therefore used traditional method  $\delta^{18}\text{O}$  values in combination with our reduction-fluorination-based  $\Delta^{17}\text{O}$  values to produce the highest-quality data set ([Supplementary Material](#), Tables S1–S3).

Our data reporting nomenclature is based on [Passey et al. \(2014\)](#) and gives the isotope value followed by the analyzed material and initial material in parentheses. For example, the  $\delta^{18}\text{O}$  of a carbonate analyzed as CO<sub>2</sub> will be reported as  $\delta^{18}\text{O}(\text{CO}_2/\text{CaCO}_3)$ , the  $\delta^{18}\text{O}$  of a water analyzed as H<sub>2</sub>O<sub>(v)</sub> will be reported as  $\delta^{18}\text{O}(\text{H}_2\text{O}_{(v)}/\text{H}_2\text{O}_{(l)})$ , and the  $\Delta^{17}\text{O}$  of a carbonate derived from O<sub>2</sub> will be reported as  $\Delta^{17}\text{O}(\text{O}_2/\text{CaCO}_3)$ . Note as well that while we presented the overview of published  $\delta^{18}\text{O}_{\text{speleothem}}$  data relative to VPDB ([Fig. 4](#)), consistent with the original publications, we normalize all data for this study to VSMOW (traditional  $\delta^{18}\text{O}$  analyses) and VSMOW-SLAP (triple oxygen isotope analyses).

### 4.2. Water sample selection and $\delta^{18}\text{O}$ analyses

Archived meteoric water samples, originally analyzed for  $\delta^{18}\text{O}$  (and in some cases  $\delta\text{D}$ ), were available from the Cave of the Bells, AZ field site (precipitation and drip water) and the Las Vegas Valley, NV (precipitation) ([Wagner et al., 2010](#); [Truebe, 2016](#); [Lachniet et al., 2017](#); [Lachniet et al., 2020](#)) ([Supplementary Material](#) text, Tables S1 and S2). We used Las Vegas Valley precipitation (610 m above sea level, asl) as analogous to that experienced at Leviathan and Lehman Caves (190 and 325 km away and at 2400 and 2080 m asl, respectively; [Lachniet et al., 2014](#)). Many water samples had been archived for 5–10 years before our analyses, so evaporation or isotopic exchange during storage was a concern. We therefore only used samples with minimal change in  $\delta^{18}\text{O}$  (<0.3‰,  $n = 2$ ) or where d-excess did not change appreciably (where data

was available, <1.2 per mil change,  $n = 3$ ). We supplemented these samples with new precipitation samples from the Las Vegas Valley ( $n = 10$ ) and from Kartchner Caverns (AZ; Fig. 4) ( $n = 4$ ), which reasonably represents Cave of the Bells (sites are 50 km apart). We analyzed samples at the University of Michigan and the University of Utah SIRFER lab using CRDS (Picarro L2130i Analyzer). At the University of Michigan, we normalized isotope compositions to the VSMOW-SLAP scale using USGS reference waters (USGS45, 46, 49, and 50) and four in-house liquid standards (MDIW2, EVAPDI, GTS, and TTNS), while the SIRFER lab used in-house liquid standards PZ and UT2, with standard EV used for quality control. The precision of standards in both labs was better than 0.1‰ and 0.3‰ for  $\delta^{18}\text{O}$  and  $\delta^2\text{H}$ , respectively. In total, the precipitation dataset comprises nineteen samples and spans the known seasonal cycle of isotopic variation, with  $\delta^{18}\text{O}$  of samples ranging from −17 to 2‰ (Wagner et al., 2010; Eastoe and Dettman, 2016; Lachniet et al., 2020).

#### 4.3. Speleothem drilling, age models, and $\delta^{18}\text{O}$ analyses

We sampled speleothem calcite to cover the range of available  $\delta^{18}\text{O}$  variability previously established in each record (Fig. 4; Supplementary Material, Table S2, Fig. S4). We needed a minimum of 30 mg of material for each sample so that we could ideally acquire four  $\Delta^{17}\text{O}$  analyses (as  $\text{O}_2$ ; ≈7 mg/analysis) and one  $\delta^{18}\text{O}$  analysis (as  $\text{CO}_2$ ; <100 µg/analysis) (see Supplementary Material for full drilling details). We aligned samples from COB-01-2, LC-1, and WR-11 following the age models presented in their respective publications (Wagner et al., 2010; Lachniet et al., 2014; Steponaitis et al., 2015). Eight samples from COB-01-2 cover 50–20 ka, ten samples from LC-1 cover the last glacial period to the present (100–0 ka, with four samples from the Holocene), seven samples from LMC-12b cover 16–6 ka, and six samples from WR-11 cover 11–4 ka.

We analyzed carbonate  $\delta^{18}\text{O}$  at the University of Michigan's Stable Isotope Lab (SIL), the Paleoclimate and Common Era lab (PACE), and the Isotopologue Paleosciences Laboratory (IPL). For SIL and PACE analyses, the analyst converted samples (70–90 µg) to  $\text{CO}_2$  using standard phosphoric acid digestion (McCreas, 1950) via a Kiel IV automated preparation device before analysis on an MAT253 mass spectrometer. We normalized  $\delta^{18}\text{O}$  values to the VSMOW scale using standards NBS-18 (7.20‰ VSMOW) and NBS-19 (28.65‰ VSMOW), with precision better than 0.1‰ ( $\delta^{13}\text{C}$  values were similarly normalized to NBS-18 = −5.09‰ and NBS-19 = 1.96‰ VPDB with precision better than 0.1‰). For IPL analyses, we converted samples (30–40 µg) to  $\text{CO}_2$  using standard phosphoric acid digestion on a clumped isotope extraction line (Passey et al., 2010; Henkes et al., 2014) before analysis on a Nu Perspective mass spectrometer. We normalized  $\delta^{18}\text{O}$  values to the VSMOW scale using standards IAEA-C2 (21.70‰ VSMOW) and ETH-1 (28.72‰ VSMOW), with precision better than 0.1‰ ( $\delta^{13}\text{C}$  values were similarly normalized

to IAEA-C2 = −8.25‰ VPDB and ETH-1 = 2.02‰ VPDB with precision better than 0.1‰).

#### 4.4. Triple oxygen isotope analyses

Our method for the  $\delta^{17}\text{O}$  and  $\delta^{18}\text{O}$  analyses used to calculate  $\Delta^{17}\text{O}$  is detailed in Passey et al. (2014), so we only present a brief overview here. We converted waters and carbonates to  $\text{O}_2$  before analysis on a Nu Perspective mass spectrometer to avoid isobaric interferences (i.e., if a carbonate is measured as  $\text{CO}_2$ , analysis of  $^{12}\text{C}^{17}\text{O}^{16}\text{O}$  is complicated by the presence of the  $^{13}\text{C}^{16}\text{O}^{16}\text{O}$  isotopologue) (e.g., Craig, 1957; Santrock et al., 1985; Brand et al., 2010; Schauer et al., 2016). For waters, we converted samples to  $\text{O}_2$  using a cobalt(III) fluoride reactor (Barkan and Luz, 2005). For carbonates, we converted samples to  $\text{CO}_2$  via acid digestion at 90 °C, reduced them to  $\text{H}_2\text{O}$  via reaction with  $\text{H}_2$  in the presence of an iron catalyst, and then converted them to  $\text{O}_2$  with the cobalt(III) fluoride reactor (Passey et al., 2014). Analytical sessions are delineated by the replacement of the cobalt(III) fluoride reactor and broken into segments if there are major changes to the system (e.g., replacement of the source filament). We used a peristaltic pump or, beginning with Reactor 15, segment 2 (Supplementary Material, Table S1), an  $\text{H}_2$ -driven continuous flow setup to pass the sample repeatedly through the reduction chamber (Passey et al., 2014). The  $\Delta^{17}\text{O}$  values of carbonate standards analyzed before and after this change in methodology are identical within error.

Our sample preparation system exhibits memory effects (Passey et al., 2014), largely localized in the cobalt(III) fluoride reactor, that we mitigated by minimizing  $\delta^{18}\text{O}$  differences between sample analyses and (primarily for waters) priming the  $\text{CoF}_3$  reactor with several injections of a sample before analysis (Supplementary Material text, Fig. S2). We accounted for isotopic drift within analytical sessions by running standard and sample replicates multiple times throughout each run. We ran at least two replicates for all water samples and attempted to run at least four replicates for all carbonate samples.

We normalized water and carbonate samples to VSMOW and SLAP analyses in each reactor segment (Supplementary Material, Table S1). For VSMOW, we defined the  $\delta^{18}\text{O}$ ,  $\delta^{17}\text{O}$ , and  $\Delta^{17}\text{O}$  values as 0‰, 0‰, and 0 per meg, respectively. For SLAP, we defined values as −55.5‰, −29.6986‰, and 0 per meg (Schoenemann et al., 2013). An alternate proposed value of  $\Delta^{17}\text{O} = -15$  per meg for SLAP (Wostbrock et al., 2020b) does not change our interpretations. We generally ran these water standards in groups of 4 replicates each on a monthly to semi-monthly basis (every ≈60–80 analyses). For sessions with more than one group of standards (i.e., multiple sets of VSMOW and SLAP replicates), we first applied a time-dependent linear correction based on the raw VSMOW mass 34/32 and 33/32 ratios to correct for instrumental drift. This correction is relatively small (≤5 per meg) and the way replicates are staggered throughout analytical sessions avoids biasing

any individual sample. Then, data were normalized to VSMOW and SLAP following Schoenemann et al. (2013).

Carbonate samples undergo acid digestion and CO<sub>2</sub> reduction steps that VSMOW and SLAP analyses do not account for, so we applied additional normalizations to δ'<sup>17</sup>O, δ'<sup>18</sup>O and Δ'<sup>17</sup>O values. This normalization is tied to the data of Wostbrock et al. (2020b), who determined values for IAEA-603 (as calcite) based on a quantitative fluorination method. First, following Passey et al. (2014), we corrected carbonate δ'<sup>18</sup>O(O<sub>2</sub>/CaCO<sub>3</sub>) values via the δ'<sup>18</sup>O(CO<sub>2</sub>/CaCO<sub>3</sub>) analyses of working standards [i.e., regressions between δ'<sup>18</sup>O(O<sub>2</sub>/CaCO<sub>3</sub>) and δ'<sup>18</sup>O(CO<sub>2</sub>/CaCO<sub>3</sub>)]. We also corrected carbonate δ'<sup>17</sup>O(O<sub>2</sub>/CaCO<sub>3</sub>) values assuming no change in Δ'<sup>17</sup>O (Passey et al. 2014). Then, we calculated mineral values for δ'<sup>17</sup>O, δ'<sup>18</sup>O and Δ'<sup>17</sup>O using fractionation factors based on the IAEA-603 values reported in Wostbrock et al. (2020b) (δ'<sup>17</sup>O = 14.83 ± 0.007‰ VSMOW2-SLAP2, δ'<sup>18</sup>O = 28.470‰ VSMOW2-SLAP2, Δ'<sup>17</sup>O = -100 ± 7 per meg VSMOW2-SLAP2) and our long-term average (δ'<sup>18</sup>O = 36.233 ± 1.24‰ VSMOW-SLAP, Δ'<sup>17</sup>O = -146 ± 15 per meg VSMOW-SLAP). These empirical fractionation factors, which account for any additional fractionation induced by the acidification and fluorination steps of our analytical methods, are <sup>17</sup>α<sub>mineral-(90°C acid, O<sub>2</sub>)</sub> = 0.9957458 and <sup>18</sup>α<sub>mineral-(90°C acid, O<sub>2</sub>)</sub> = 0.9918723 [θ<sub>mineral-(90°C acid, O<sub>2</sub>)</sub> = 0.5224]. Last, we corrected for temporal drift in Δ'<sup>17</sup>O(O<sub>2</sub>/CaCO<sub>3</sub>) using an offset correction defined by the observed and defined values of IAEA-603 (reactors 14–16) and IAEA-C1 (reactors 10–16) (both values defined as -100 per meg VSMOW-SLAP; Wostbrock et al., 2020b). It is reasonable to expect that the two standards have similar isotopic composition given their provenance (IAEA, 2021). Correspondingly, in this study we found gas analyte values for IAEA-603 (*n* = 22) of δ'<sup>18</sup>O(O<sub>2</sub>/CaCO<sub>3</sub>) = 35.934 ± 1.438‰ VSMOW-SLAP and Δ'<sup>17</sup>O(O<sub>2</sub>/CaCO<sub>3</sub>) = -148 ± 17 per meg VSMOW-SLAP and values for IAEA-C1 (*n* = 48) of δ'<sup>18</sup>O(O<sub>2</sub>/CaCO<sub>3</sub>) = 36.370 ± 1.076‰ VSMOW-SLAP and Δ'<sup>17</sup>O(O<sub>2</sub>/CaCO<sub>3</sub>) = -145 ± 14 per meg VSMOW-SLAP. Reported as mineral values with the temporal drift correction for Δ'<sup>17</sup>O, we found values for IAEA-603 (*n* = 22) of δ'<sup>18</sup>O(O<sub>2</sub>/CaCO<sub>3</sub>) = 27.801 ± 1.476‰ VSMOW-SLAP and Δ'<sup>17</sup>O(O<sub>2</sub>/CaCO<sub>3</sub>) = -100 ± 9 per meg VSMOW-SLAP and values for IAEA-C1 (*n* = 48) of δ'<sup>18</sup>O(O<sub>2</sub>/CaCO<sub>3</sub>) = 28.195 ± 1.051‰ VSMOW-SLAP and Δ'<sup>17</sup>O(O<sub>2</sub>/CaCO<sub>3</sub>) = -100 ± 8 per meg VSMOW-SLAP (Supplementary Material, Table S1).

We assessed the repeatability of our Δ'<sup>17</sup>O analyses with water and carbonate standards that were not used in the data normalization procedures above. For waters, we measured standard water USGS-46 as an unknown. Our long term Δ'<sup>17</sup>O value for USGS-46 is 18 ± 10 per meg VSMOW-SLAP, whereas in this study we observed a value of 17 ± 10 per meg VSMOW-SLAP (*n* = 27). For carbonates, in-house standard 102-GC-AZ01 had a Δ'<sup>17</sup>O value of -67 ± 10 VSMOW-SLAP (*n* = 81) during this study (this also defines our long-term average). We report analytical results for all reference materials in the Supplementary

Material, which will allow for retrospective normalization using alternative schemes (Supplementary Material, Table S1).

#### 4.5. Estimation of θ<sub>CaCO<sub>3</sub>-H<sub>2</sub>O</sub> and reconstructing formation water isotope composition

Reconstructing formation water triple oxygen isotope composition from measured δ'<sup>18</sup>O(CO<sub>2</sub>/CaCO<sub>3</sub>) and Δ'<sup>17</sup>O(O<sub>2</sub>/CaCO<sub>3</sub>) requires knowledge of speleothem formation temperature, α'<sup>18</sup><sub>CaCO<sub>3</sub>-H<sub>2</sub>O</sub>, and θ<sub>CaCO<sub>3</sub>-H<sub>2</sub>O</sub> (used to calculate α'<sup>17</sup><sub>CaCO<sub>3</sub>-H<sub>2</sub>O</sub> after Eq. (4); see also Supplementary Material, Matlab Code). We calculated α'<sup>18</sup><sub>CaCO<sub>3</sub>-H<sub>2</sub>O</sub> at modern cave temperature (Cave of the Bells = 19 °C, Leviathan Cave = 8.2 °C, and Lehman Caves = 11 °C; Wagner et al., 2010; Lachniet et al., 2014; Steponaitis et al., 2015) using the calcite calibration of Kim and O'Neil (1997). For θ<sub>CaCO<sub>3</sub>-H<sub>2</sub>O</sub>, several theoretical and experimental estimates exist that converge on a value of 0.524–0.526 for most Earth surface conditions (≈0–30 °C) (Cao and Liu, 2011; Hayles et al., 2018; Guo and Zhou, 2019b; Wostbrock et al., 2020a; Schauble and Young, 2021; Sharp and Wostbrock, 2021; Bergel et al., 2020; Voarintsoa et al., 2020).

We added to these estimates with a suite of synthetic carbonates grown at equilibrium conditions (5, 15, and 35 °C, see Supplementary Material for additional details). Our method for precipitating carbonate largely followed that of Ghosh et al., 2006 and Zaarur et al., 2013 (see also, e.g., Kim and O'Neil, 1997; Wostbrock et al., 2020b and the compilation of sources therein). We added ≈75% of the maximum solubility of calcite to 1-L of water in plastic-capped Erlenmeyer flasks and placed these in water baths held at constant experimental temperature (±0.3 °C) using Inkbird ITC-308 Digital Temperature Controllers. We bubbled CO<sub>2</sub> through the system until calcite visibly dissolved and then kept the solution under constant temperature to allow isotopic equilibrium to establish (e.g., Beck et al., 2005). We precipitated calcite by bubbling nitrogen directly into the solutions at a rate of ≈3 bubbles/s for two minutes per day, after which we capped and shook the flask. Calcite formed slowly, with the 5, 15, and 35 °C flasks taking four, five, and two weeks, respectively, for substantial calcite to form. We verified that evaporation did not influence samples through no change in the water level and comparing water δ'<sup>18</sup>O and δD before and after purging with nitrogen.

Our samples give an average value of θ<sub>CaCO<sub>3</sub>-H<sub>2</sub>O</sub> = 0.5250 ± 0.0002 (Table 1; Fig. 5; Supplementary Material, Table S6). For comparison, we also renormalized data from Passey et al. (2014) and Sha et al. (2020), Bergel et al. (2020), and Voarintsoa et al. (2020) to the Wostbrock et al. (2020b) mineral values used here [Fig. 5, Tables S7–S9; see renormalization procedures in the next section, 4.6 Renormalization of prior triple oxygen isotope data]. In this normalization scheme, the Sha et al. (2020) modern speleothem-drip water pairs give θ<sub>CaCO<sub>3</sub>-H<sub>2</sub>O</sub> = 0.5251 ± 0.0003 (formation at 17 ± 1 °C), the Passey et al. (2014) combined values for eggshells, a mollusk shell, and coral sample

Table 1  
Data summary for equilibrium-grown calcites and associated waters.

Experiment ID	Growth temperature (°C)	Water sample ID	Sample type	# replicates	$\delta^{17}\text{O}(\text{O}_2/\text{H}_2\text{O})$ (‰, VSMOW-VSLAP)	$\delta^{18}\text{O}(\text{O}_2/\text{H}_2\text{O})$ (‰, VSMOW-VSLAP)	$\Delta^{17}\text{O}(\text{O}_2/\text{H}_2\text{O})$ (per meg, VSMOW-VSLAP, $\lambda = 0.528$ ) <sup>1</sup>	1 SEM	1 SEM	1 SEM	$\delta^{18}\text{O}(\text{H}_2\text{O}_{(v)}/\text{H}_2\text{O}_{(l)})$ (‰, VSMOW)	$\delta\text{D}(\text{H}_2\text{O}_{(v)}/\text{H}_2\text{O}_{(l)})$ (‰, VSMOW)	1σ $\delta^{18}\text{O}$	1σ $\delta\text{D}$
Experiment ID	Growth temperature (°C)	Carbonate sample ID	Sample type	# replicates	$\delta^{17}\text{O}(\text{O}_2/\text{CaCO}_3)$ (‰, VSMOW-VSLAP)	$\delta^{18}\text{O}(\text{O}_2/\text{CaCO}_3)$ (‰, VSMOW-VSLAP)	$\Delta^{17}\text{O}(\text{O}_2/\text{CaCO}_3)$ (per meg, VSMOW-VSLAP, $\lambda = 0.528$ ) <sup>1</sup>	1 SEM	1 SEM	1 SEM	$\delta^{13}\text{C}(\text{CO}_2/\text{CaCO}_3)$ (‰, VSMOW)	$\delta^{18}\text{O}(\text{CO}_2/\text{CaCO}_3)$ (‰, VSMOW)	1σ $\delta^{13}\text{C}$	1σ $\delta^{18}\text{O}$
5-3	5	D17OEQ 5-3 3.17.2020	water	5	-3.589	-6.809	6	0.136	0.251	4	-6.786	-47.276	0.1	0.3
5-4	5	D17OEQ 5-4 3.17.2020	water	2	-3.483	-6.616	10	0.040	0.068	4	-6.595	-46.302	0.1	0.3
15-1	15	D17OEQ 15-1 3.2.2020	water	5	-3.437	-6.525	9	0.045	0.082	2	-6.504	-46.217	0.1	0.3
35-1	35	D17OEQ 35-1 3.4.2020	water	5	-3.420	-6.492	8	0.105	0.192	3	-6.471	-47.797	0.1	0.3
Experiment ID	Growth temperature (°C)	17 $\alpha_{\text{calcite}-\text{water}}$ <sup>2</sup>	18 $\alpha_{\text{calcite}-\text{water}}$ <sup>3</sup>	θ <sub>calcite-water</sub>										
5-3	5	1.017540	1.033671	0.5251										
5-4	5	1.017584	1.033761	0.5250										
15-1	15	1.016023	1.030757	0.5247										
35-1	35	1.013906	1.026643	0.5252										
<b>Average</b>		<b>1.0163</b>	<b>1.0312</b>	<b>0.5250</b>										
<b>1σ</b>		<b>0.0017</b>	<b>0.0033</b>	<b>0.0002</b>										

<sup>1</sup> Normalized to IAEA-603 and IAEA-C1 = -100 per meg (Wostbrock et al., 2020b).

<sup>2</sup> Calculated using traditional  $\delta^{18}\text{O}$  analyses (on water vapor and  $\text{CO}_2$ ) and  $\text{O}_2$ -based  $\Delta^{17}\text{O}$  analyses.

<sup>3</sup> Calculated using traditional  $\delta^{18}\text{O}$  analyses (on water vapor and  $\text{CO}_2$ ).

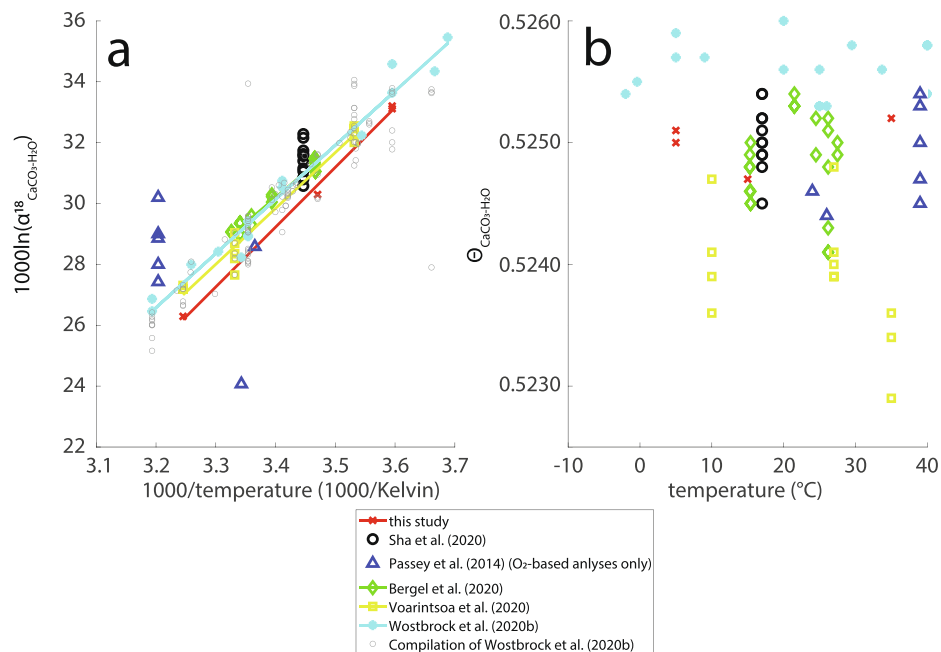


Fig. 5. Measured values for isotopic fractionation occurring during the calcite-water reaction. (a) The relationship between  $1000\ln(\alpha^{18}\text{CaCO}_3-\text{H}_2\text{O})$  and experimental temperature (as  $1000/\text{K}$ ). Data from this study are the red x's, Sha et al. (2020) data are black circles, Passey et al. (2014) data are blue triangles (note the scatter is likely due to these being  $\text{O}_2$ -based analyses; see Section 4.4 *Triple oxygen isotope analyses* for details), Bergel et al., 2020 data are green diamonds, Voarintsoa et al., 2020 data are yellow squares, and Wostbrock et al., 2020a data are light blue dots. Triple oxygen isotope data are renormalized to the Wostbrock et al. (2020b) mineral values (Passey et al. 2014; Sha et al., 2020; Bergel et al., 2020; Kim et al., 2007; Kim et al., 2015; Wostbrock et al., 2020b; Voarintsoa et al., 2020; Supplementary Material, Tables S7–S10). For comparison, the compilation of Wostbrock et al., (2020a) is the light gray circles. Best fit lines are shown for data with significant temperature spread, but a line is not shown for the Passey et al. (2014) data as the  $\text{O}_2$ -based analyses are not precise enough for useful comparison. (b) Estimates of  $\theta_{\text{CaCO}_3-\text{H}_2\text{O}}$  vs. experimental temperature ( $^{\circ}\text{C}$ ), with symbols and colors as in panel (a).

give  $\theta_{\text{CaCO}_3-\text{H}_2\text{O}} = 0.5248 \pm 0.0004$  (formation at 39, 24, and  $26^{\circ}\text{C}$ , respectively), the Bergel et al. (2020) values for freshwater mollusks give  $\theta_{\text{CaCO}_3-\text{H}_2\text{O}} = 0.5248 \pm 0.0004$  (formation at  $15\text{--}28^{\circ}\text{C}$ ), and the Voarintsoa et al. (2020) values for inorganic calcite and aragonite precipitations give  $\theta_{\text{CaCO}_3-\text{H}_2\text{O}} = 0.5239 \pm 0.0005$  (formation at  $15\text{--}28^{\circ}\text{C}$ ).

Our new data and the renormalized data support  $\theta_{\text{CaCO}_3-\text{H}_2\text{O}} = 0.524\text{--}0.526$ , but differences in the fourth decimal place are important for accurate reconstructions and cause 10 s per meg differences in reconstructed formation water  $\Delta^{17}\text{O}$ . We therefore temporarily accept the average of values from Passey et al., 2014, Sha et al., 2020, and this study ( $\theta_{\text{CaCO}_3-\text{H}_2\text{O}} = 0.5250 \pm 0.0003$ ;  $n = 22$ ) as most internally consistent and relevant for reconstructing speleothem formation water  $\Delta^{17}\text{O}$ . Regardless, other definitions for  $\alpha^{18}\text{CaCO}_3-\text{H}_2\text{O}$  or  $\theta_{\text{CaCO}_3-\text{H}_2\text{O}}$  (e.g., Kim and O'Neil, 1997; Coplen, 2007; Affek and Zaarur, 2014; Wostbrock et al., 2020b; Bergel et al., 2020; Voarintsoa et al., 2020) would not affect overall trends of reconstructed formation waters in  $\Delta^{17}\text{O}$  vs.  $\delta^{18}\text{O}$  space (Supplementary Material, Matlab Code). However, they would affect absolute values of reconstructed formation waters. For example, use of the Wostbrock et al. (2020b) calibrations for  $\theta_{\text{CaCO}_3-\text{H}_2\text{O}}$  and  $\alpha^{18}\text{CaCO}_3-\text{H}_2\text{O}$  would yield  $\Delta^{17}\text{O}$  values 10–30 per meg lower than we report.

In addition, while many of our samples are Holocene in age and likely formed at similar temperatures to modern, those formed during the last glacial period likely experi-

enced significantly lower temperatures (e.g., Stute et al., 1995; Reinemann et al., 2009; Marchetti et al., 2011; Barth et al. 2016; Harbert and Nixon, 2018; Huth et al., 2020; Quirk et al., 2020) that are harder to constrain. A temperature uncertainty of  $\pm 5^{\circ}\text{C}$  translates to an uncertainty in reconstructed water  $\delta^{18}\text{O}$  of  $\approx 1\text{‰}$  (e.g., Kim and O'Neil, 1997) and in  $\Delta^{17}\text{O}$  of  $\approx 5$  per meg (i.e., within analytical error). Given that pre-Holocene samples likely formed at colder temperatures than their Holocene counterparts, reconstructed  $\delta^{18}\text{O}$  values will be underestimated and  $\Delta^{17}\text{O}$  values will be slightly overestimated. Regardless of this error, the broad-scale patterns we interpret do not depend on specific knowledge of the formation temperature, as demonstrated by a Monte Carlo simulation with temperature ranges of, as compared to modern,  $\pm 2^{\circ}\text{C}$  for Holocene samples and  $-15$  to  $-5^{\circ}\text{C}$  for pre-Holocene samples (Supplementary Material text, Fig. S5) (e.g., Stute et al., 1995; Reinemann et al., 2009; Marchetti et al., 2011; Barth et al. 2016; Harbert and Nixon, 2018; Huth et al., 2020; Quirk et al., 2020).

#### 4.6. Renormalization of prior triple oxygen isotope data

We renormalized data from Passey et al. (2014), Sha et al. (2020), Bergel et al. (2020), and Voarintsoa et al. (2020) to allow direct comparison with prior estimates of  $\theta_{\text{CaCO}_3-\text{H}_2\text{O}}$  and speleothem triple oxygen isotope data (Sha et al. 2020).

#### 4.6.1. Renormalization of Passey et al. (2014) data

Renormalizing the data of Passey et al. (2014) to the values of Wostbrock et al. (2020b) largely followed the same procedure as this study, except that we corrected samples to the mineral value of NBS-19 (note that IAEA-603 is intended to replace NBS-19; IAEA, 2021) (Supplementary Material, Table S9). Wostbrock et al. (2020b) give values for NBS-19 of  $\delta^{17}\text{O} = 14.923 \pm 0.010\text{\textperthousand}$  VSMOW2-SLAP2,  $\delta^{18}\text{O} = 28.650\text{\textperthousand}$  VSMOW2-SLAP2,  $\Delta^{17}\text{O} = -10.2 \pm 10$  per meg VSMOW2-SLAP2. The empirical fractionation factors used to account for any additional fractionation induced by the acidification and fluorination steps of our analytical methods are  ${}^{17}\alpha_{\text{mineral}-(90^\circ\text{C acid, O}_2)} = 0.9957782$  and  ${}^{18}\alpha_{\text{mineral}-(90^\circ\text{C acid, O}_2)} = 0.9919498$  [ $\theta_{\text{mineral}-(90^\circ\text{C acid, O}_2)} = 0.5234$ ] (note samples were analyzed on a different instrument at Johns Hopkins University). For the temporal drift correction, not all sessions for the Passey et al. (2014) data had NBS-19 analyses. In these cases, we corrected to the long-term average of internal standard Tank CO<sub>2</sub> ( $\Delta^{17}\text{O} = -77 \pm 6$  per meg VSMOW2-SLAP2), as identified from reactors with analyses of both Tank CO<sub>2</sub> and NBS-19 (Supplementary Material, Table S9).

#### 4.6.2. Renormalization of Sha et al. (2020) data

We renormalized the Sha et al. (2020) carbonate data (their Tables 4–6) to the Wostbrock et al. (2020b) mineral values for NBS-18 and IAEA-603 (Supplementary Material, Table S7; note we did not renormalize water data, which was already calibrated to VSMOW-SLAP). Sha et al. (2020) reported measured values (for some samples, their Table 4) and normalized values (their Tables 4–6) of  $\delta^{17}\text{O}$ ,  $\delta^{18}\text{O}$ , and  $\Delta^{17}\text{O}$  for waters and speleothems. They determined that their measured  $\delta^{18}\text{O}$  values for standards NBS-18 and IAEA-603 (17.481 and 39.092‰ VSMOW, respectively) were within error of the accepted values (17.506 and 39.002‰ VSMOW, respectively) and applied no further correction (i.e., measured and normalized  $\delta^{18}\text{O}$  values are the same). To acquire measured  $\delta^{17}\text{O}$  values for all samples, we inferred the parameters used in the two-point normalization scheme of Sha et al. (2020) (i.e., we developed a linear regression between samples with both measured and normalized  $\delta^{17}\text{O}$  data reported) and used these to calculate measured  $\delta^{17}\text{O}$  from normalized  $\delta^{17}\text{O}$  (Supplementary Material, Table S7). We used the measured and normalized  $\delta^{17}\text{O}$  values to infer the normalization parameters for two reasons. First, based on their reported data (their Table 4), we inferred that Sha et al., 2020 used a  $\delta^{17}\text{O}$  value for IAEA-603 of 20.256‰ VSMOW instead of the reported 20.218‰ VSMOW. Correcting for this would lower sample  $\Delta^{17}\text{O}$  values by 16–37 per meg. Second, Sha et al., 2020 define accepted  $\delta^{18}\text{O}$  values for standards as IAEA-recommended mineral values, but define  $\delta^{17}\text{O}$  and  $\Delta^{17}\text{O}$  values based on CO<sub>2</sub> extractions (Barkan et al., 2019). While Barkan et al., 2019 also start from IAEA recommended values in defining accepted  $\delta^{18}\text{O}$  values for standards, they additionally account for fractionation occurring during acid digestion (at 25 °C) in their definition to make the values directly comparable to their analyses of CO<sub>2</sub> extracted from carbonates. The difference

in these  $\delta^{18}\text{O}$  definitions is significant if  $\delta^{18}\text{O}$  data are also corrected with a two-point normalization scheme, increasing sample  $\Delta^{17}\text{O}$  by 4–35 per meg. Note, however, that the combined effect of these changes is small, producing  $\Delta^{17}\text{O}$  values  $\leq 12$  per meg more negative than reported in Sha et al. (2020) (their Tables 4–6). After calculating measured  $\delta^{17}\text{O}$  values for all data, and following the approach used in this study, we developed a new two-point normalization scheme for  $\delta^{17}\text{O}$  and  $\delta^{18}\text{O}$  data using the measured NBS-18 and IAEA-603 values reported by Sha et al. (2020) and the corresponding mineral values of Wostbrock et al. (2020b) (Supplementary Material, Tables S7 and S8; an example calculation is supplied in the Supplementary Material, Matlab Code). We set the accepted standard  $\Delta^{17}\text{O}$  values to IAEA-603 = −100 per meg and NBS-18 = −48 per meg,  $\delta^{18}\text{O}$  values to the accepted IAEA (International Atomic Energy Agency) values (28.470 and 7.200‰ VSMOW, respectively), and then calculated standard  $\delta^{17}\text{O}$  values following Eq. (2) (14.831 and 3.747‰ VSMOW, respectively). Finally, following the procedure outlined above (section 4.5 Estimation of  $\theta_{\text{CaCO}_3-\text{H}_2\text{O}}$  and reconstructing formation water isotope composition) we reconstructed formation water isotope composition using the preferred temperature estimates of Sha et al. (2020) (their Table 8; Supplementary Material, Table S8).

#### 4.6.3. Renormalization of Bergel et al. (2020) and Voarintsoa et al. (2020) data

We renormalized data from Bergel et al. (2020) and Voarintsoa et al. (2020) to the Wostbrock et al. (2020b) mineral values for NBS-18 and IAEA-603 (Supplementary Material, Table S10; again, we did not renormalize water data, which was already calibrated to VSMOW-SLAP). We developed a two-point normalization scheme for  $\delta^{17}\text{O}$  and  $\delta^{18}\text{O}$  data using the measured CO<sub>2</sub> values of NBS-18 and IAEA-603 reported by Barkan et al. (2019) and the corresponding CO<sub>2</sub> values of Wostbrock et al. (2020b) (Supplementary Material, Table S10; an example calculation is supplied in the Supplementary Material, Matlab Code). We set the accepted standard  $\Delta^{17}\text{O}$  values to IAEA-603 = −147 per meg and NBS-18 = −100 per meg,  $\delta^{18}\text{O}$  values to the accepted IAEA (International Atomic Energy Agency) values (39.012 and 17.524‰ VSMOW, respectively), and then calculated standard  $\delta^{17}\text{O}$  values following Eqn. 2 (20.262 and 9.114‰ VSMOW, respectively). We converted data from CO<sub>2</sub> values to mineral values by applying an acid fractionation factor. Following Voarintsoa et al. (2020), for  $\delta^{18}\text{O}$  data we used a mixing model to account for the mixed aragonite-calcite samples and acquire an overall  ${}^{18}\alpha_{\text{acid}}$  for each sample (for digestion at 25 °C,  ${}^{18}\alpha_{\text{aragonite}} = 1.01063$  and  ${}^{18}\alpha_{\text{calcite}} = 1.01025$ ; Kim et al. (2015); Kim et al. (2007)). For  $\delta^{17}\text{O}$  data, we calculated  ${}^{17}\alpha_{\text{acid}}$  for each sample using the Wostbrock et al. (2020b) value for  $\theta_{\text{acid}}$ . 0.5230.

## 5. RESULTS

### 5.1. Modern water isotope composition

In the samples analyzed here, modern precipitation from Cave of the Bells and Kartchner Caverns, AZ ( $n = 10$ )

Table 2  
Summary of speleothem and associated water triple oxygen isotope data, traditional stable isotope data, ages, and metadata.

Speleothem ID	Sample ID	# replicates	$\delta^{17}\text{O(O}_2/\text{CaCO}_3)$ (‰, VSMOW-VSLAP)	$\delta^{18}\text{O(O}_2/\text{CaCO}_3)$ (‰, VSMOW-VSLAP)	$\Delta^{17}\text{O(O}_2/\text{CaCO}_3$ (per meg, VSMOW-VSLAP, $\lambda = 0.528$ ) <sup>1</sup>	1 SEM $\delta^{17}\text{O}$	1 SEM $\delta^{18}\text{O}$	1 SEM $\Delta^{17}\text{O}$	age (yr BP) <sup>2</sup>	$\delta^{13}\text{C(CO}_2/\text{CaCO}_3$ (‰, VPDB)	$\delta^{18}\text{O(CO}_2/\text{CaCO}_3$ (‰, VSMOW)	$1\sigma \delta^{13}\text{C}$	$1\sigma \delta^{18}\text{O}$
<i>Cave of the Bells</i>													
COB-01-02	COB-0102-25.5-21.5	4	10.163	19.381	-71	0.130	0.249	4	19,814	-7.7	19.6	0.05	0.09
COB-01-02	COB-0102-46.2	4	10.640	20.302	-80	0.137	0.257	3	37,962	-8.0	20.6	0.05	0.09
COB-01-02	COB-0102-60	4	10.471	19.991	-84	0.063	0.117	3	40,551	-7.7	19.8	0.05	0.09
COB-01-02	COB-0102-88.6	4	10.793	20.607	-88	0.210	0.391	4	46,313	-7.6	21.0	0.05	0.09
COB-01-02	COB-0102-99.6	4	10.137	19.361	-86	0.160	0.297	3	47,375	-6.3	19.7	0.05	0.09
COB-01-02	COB-0102-107.7	4	10.593	20.225	-86	0.311	0.586	5	49,403	-7.2	20.9	0.05	0.09
COB-01-02	COB-0102-112.8	4	11.156	21.272	-75	0.312	0.587	5	51,018	-5.3	22.0	0.05	0.09
COB-01-02	COB-0102-55KYR	3	11.273	21.512	-85	0.141	0.268	3	52,173	-6.9	21.9	0.05	0.09
<i>Leviathan Cave</i>													
LC-1	LC-1-0-2	4	9.606	18.343	-79	0.204	0.387	2	45	-4.9	19.0	0.05	0.06
LC-1	LC-1-37.5-39.5	5	9.965	19.008	-71	0.348	0.654	4	1043	-4.1	19.4	0.05	0.06
LC-1	LC-1-164-168	4	10.916	20.823	-79	0.128	0.238	2	8534	-2.3	20.7	0.05	0.06
LC-1	LC-1-181.5-183	4	9.544	18.218	-75	0.398	0.749	3	12,158	-1.2	19.0	0.05	0.06
LC-1	LC-1-192-193.5	4	8.568	16.363	-71	0.710	1.343	7	34,632	-1.4	17.9	0.05	0.06
LC-1	LC-1-236.5-238.5	4	9.953	18.980	-68	0.217	0.417	5	49,194	-2.3	18.3	0.05	0.06
LC-1	LC-1-305-307.5	4	9.780	18.671	-78	0.366	0.690	3	75,583	-2.1	18.6	0.05	0.06
LC-1	LC-1-376-378	4	10.548	20.119	-75	0.100	0.186	6	81,001	-2.1	20.0	0.05	0.06
LC-1	LC-1-429-430.5	4	9.617	18.357	-76	0.440	0.826	4	87,625	-1.7	18.7	0.05	0.06
LC-1	LC-1-508.5-511.5	4	10.550	20.144	-86	0.102	0.188	3	101,486	-0.8	20.6	0.05	0.06
<i>Lehman Caves</i>													
LMC-12b	LMC-12b-4-5	3	10.668	20.373	-89	0.717	1.348	5	6204	-0.9	21.5	0.05	0.06
LMC-12b	LMC-12b-9-10	1	13.322	25.409	-93	-	-	-	7075	8.9	25.6	0.05	0.06
LMC-12b	LMC-12b-12-13	3	12.805	24.429	-94	0.047	0.086	2	7834	6.7	24.8	0.05	0.06
LMC-12b	LMC-12b-15-17	4	12.366	23.597	-93	0.220	0.415	2	9097	2.8	23.4	0.05	0.06
LMC-12b	LMC-12b-21-22	4	12.518	23.886	-94	0.198	0.374	1	11,400	6.8	24.3	0.05	0.06
LMC-12b	LMC-12b-29.5-30.5	4	11.107	21.189	-81	0.472	0.889	3	14,084	1.0	21.6	0.05	0.06
LMC-12b	LMC-12b-36-37	4	10.802	20.606	-78	0.518	0.980	3	15,779	-1.8	21.0	0.05	0.06
WR-11	WR-11-0-1	4	9.748	18.617	-82	0.446	0.842	2	4095	-2.4	19.8	0.05	0.06
WR-11	WR-11-7-8	4	10.421	19.886	-79	0.264	0.504	3	5212	-2.0	20.1	0.05	0.06
WR-11	WR-11-17-18	4	10.017	19.130	-83	0.229	0.438	3	7106	-2.6	19.0	0.05	0.06
WR-11	WR-11-21-22	4	9.618	18.368	-80	0.511	0.962	5	7765	-1.9	19.7	0.05	0.06
WR-11	WR-11-33.5-34.5	4	8.887	16.971	-73	0.371	0.708	8	8969	-4.1	18.5	0.05	0.06
WR-11	WR-11-60.5-61.5	4	9.999	19.078	-74	0.324	0.612	5	11,114	-3.3	18.7	0.05	0.06

Table 2 (continued).

Water site ID <sup>3</sup>	Sample ID	# replicates	$\delta^{17}\text{O}(\text{O}_2/\text{H}_2\text{O})$ (‰, VSMOW-VSLAP)	$\delta^{18}\text{O}(\text{O}_2/\text{H}_2\text{O})$ (‰, VSMOW-VSLAP)	$\Delta^{17}\text{O}(\text{O}_2/\text{H}_2\text{O})$ (per meg, VSMOW-VSLAP, $\lambda = 0.528$ )	1 SEM $\delta^{17}\text{O}$	1 SEM $\delta^{18}\text{O}$	1 SEM $\Delta^{17}\text{O}$	collection date	$\delta^{18}\text{O}(\text{H}_2\text{O}_{(v)}/\text{H}_2\text{O}_{(l)})$ (‰, VSMOW) <sup>4</sup>	$\delta\text{D}(\text{H}_2\text{O}_{(v)}/\text{H}_2\text{O}_{(l)})$ (‰, VSMOW) <sup>4</sup>	1σ $\delta^{18}\text{O}$	1σ $\delta\text{D}$
<i>Cave of the Bells-Popcorn Room (drip water)</i>													
COB-PR	COB-PR-6FEB11	3	-4.001	-7.610	17	0.278	0.526	4	06-02-2011	-8.9	-61.2	0.1	0.3
COB-PR	COB-PR-20AUG11	3	-4.199	-8.009	29	0.195	0.359	6	20-08-2011	-8.9	-61.2	0.1	0.3
<i>Cave of the Bells-Rain Gauge</i>													
COB-RG	COB-RG-13JUL06	4	-0.726	-1.389	7	0.232	0.429	7	13-07-2006	-2.3	-11.4	0.1	0.3
COB-RG	COB-RG-20AUG06	4	-2.535	-4.810	5	0.287	0.540	3	20-08-2006	-5.6	-37.4	0.1	0.3
COB-RG	COB-RG-19NOV06	4	-2.429	-4.602	1	0.299	0.557	5	19-11-2006	-5.5	-46.9	0.1	0.3
<i>Nevada-Las Vegas Valley (precipitation)</i>													
NV-UNLV	NV-19-10003	2	-3.907	-7.426	14	0.053	0.104	2	06-03-2019	-7.8	-62.7	0.1	0.3
NV-UNLV	NV-19-10008	2	-3.098	-5.851	-9	0.019	0.036	0	21-04-2019	-6.2	-61.3	0.1	0.3
NV-UNLV	NV-19-10012	2	-5.399	-10.267	21	0.004	0.002	3	10-05-2019	-10.8	-79.0	0.1	0.3
NV-UNLV	NV-19-10015	2	0.864	1.675	-21	0.015	0.031	1	31-07-2019	1.7	1.3	0.1	0.3
NV-UNLV	NV-19-10026	2	-8.386	-15.926	23	0.075	0.149	4	27-12-2019	-17.1	-128.5	0.1	0.3
NV-UNLV	NV-19-10030	2	-4.378	-8.317	14	0.006	0.010	0	10-02-2020	-8.6	-60.8	0.1	0.3
NV-UNLV	NV-19-10037	2	-4.938	-9.414	33	0.032	0.054	3	21-03-2020	-9.8	-65.0	0.1	0.3
NV-UNLV	NV-19-1004	2	-2.896	-5.506	11	0.001	0.000	1	11-03-2019	-5.9	-44.6	0.1	0.3
NV-UNLV	NV-19-10041	2	1.074	2.115	-43	0.047	0.098	5	21-04-2020	1.8	-12.0	0.1	0.3
NV-UNLV	NV-19-10047	2	-6.058	-11.547	39	0.010	0.026	4	07-11-2020	-12.0	-86.0	0.1	0.3
<i>Kartchner Caverns-Rain Gauge</i>													
KRC-RG	KRC-RG-6JUL20	2	-4.664	-8.852	10	0.038	0.069	1	06-07-2020	-9.2	-79.1	0.1	0.3
KRC-RG	KRC-RG-19JUL20	2	-1.534	-2.867	-20	0.103	0.209	8	19-07-2020	-3.5	-30.2	0.1	0.3
KRC-RG	KRC-RG-3AUG20	2	-1.068	-2.029	3	0.022	0.028	7	03-08-2020	-3.7	-21.6	0.1	0.3
KRC-RG	KRC-RG-13Aug20	2	-1.213	-2.291	-4	0.004	0.006	1	13-08-2020	-2.8	-23.7	0.1	0.3

<sup>1</sup> Normalized to IAEA-603 and IAEA-C1 = -100 per meg (Wostbrock et al., 2020b).<sup>2</sup> Age models follow the original publication (note LMC-12b is presented new here). Wagner et al (2010) uses a spline for the section covered here. All other samples are assigned ages based on linear interpolation between nearest dates.<sup>3</sup> See Supplementary Materials, Table S4 for data of reanalyzed archived water samples that were rejected based on changes in  $\delta^{18}\text{O}$  and/or d-excess values (not all samples were originally analyzed for  $\delta\text{D}$ ).<sup>4</sup> Data is from this study. See Supplementary Materials, Table S4 for comparison with original analyses.

spans  $\delta^{18}\text{O}(\text{H}_2\text{O}_{(\text{v})}/\text{H}_2\text{O}_{(\text{l})}) = -9.2\text{--}4.5\text{\textperthousand}$  VSMOW-SLAP and  $\Delta^{17}\text{O}(\text{O}_2/\text{H}_2\text{O}) = -20$  to 10 per meg VSMOW-SLAP while drip water ( $n = 10$ ) both have  $\delta^{18}\text{O}(\text{H}_2\text{O}_{(\text{v})}/\text{H}_2\text{O}_{(\text{l})}) = -8.9\text{\textperthousand}$  VSMOW-SLAP and span  $\Delta^{17}\text{O}(\text{O}_2/\text{H}_2\text{O}) = 17\text{--}29$  per meg VSMOW-SLAP. Modern precipitation from the Las Vegas Valley, NV spans  $\delta^{18}\text{O}(\text{H}_2\text{O}_{(\text{v})}/\text{H}_2\text{O}_{(\text{l})}) = -17.1$  to  $1.8\text{\textperthousand}$  VSMOW-SLAP and  $\Delta^{17}\text{O}(\text{O}_2/\text{H}_2\text{O}) = -43$  to 39 per meg VSMOW-SLAP. Precipitation data from these locations show coherent variability in  $\Delta^{17}\text{O}$  vs.  $\delta^{18}\text{O}$  space (Fig. 2f, Table 2; see also an expanded version of Table 2 in Supplementary Material, Table S2). Consistent with previous analyses, warm season precipitation  $\delta^{18}\text{O}$  values are higher than their cool season counterparts (Wagner et al., 2010; Eastoe and Dettman, 2016; Lachniet et al., 2020). Conversely, warm season precipitation  $\Delta^{17}\text{O}$  values are lower than their cool season counterparts. Drip water  $\delta^{18}\text{O}(\text{H}_2\text{O}_{(\text{v})}/\text{H}_2\text{O}_{(\text{l})})$  and  $\Delta^{17}\text{O}(\text{O}_2/\text{H}_2\text{O})$  values from Cave of the Bells are consistent with the cool season precipitation data. Combined, the modern water data define a local meteoric water line (LMWL) of  $\Delta^{17}\text{O}(\text{O}_2/\text{H}_2\text{O}) = -3.6 \times \delta^{18}\text{O}(\text{H}_2\text{O}_{(\text{v})}/\text{H}_2\text{O}_{(\text{l})}) - 16.7$  ( $r^2 = 0.69$ ) and a triple isotope ( $\delta^{17}\text{O}$  vs.  $\delta^{18}\text{O}$ ) slope of 0.5244 (Table 3). The modern water isotope data fall within the range of unevaporated meteoric water samples (tap, stream, and river water) reported for the western USA (Li et al., 2015; Aron et al., 2021; Bershaw et al., 2020).

## 5.2. Speleothem isotope composition

The  $\delta^{18}\text{O}(\text{CO}_2/\text{CaCO}_3)$  data from Cave of the Bells range from 19.6 to 22.0‰ VSMOW and are consistent with those from the higher resolution  $\delta^{18}\text{O}$  record (Fig. 4) (Wagner et al., 2010). The  $\Delta^{17}\text{O}(\text{O}_2/\text{CaCO}_3)$  data range from -88 to -71 per meg (Fig. 6a). The data show no trend when plotted in  $\Delta^{17}\text{O}$  vs.  $\delta^{18}\text{O}$  space (slope -0.79,  $r^2 = 0.01$ ) and are inconsistent with a single isotope forcing from cave kinetics (7 per meg/‰;  $p = 0.03$ ) (see Table 3 for line statistics and results for all test slopes).

The  $\delta^{18}\text{O}(\text{CO}_2/\text{CaCO}_3)$  data from Leviathan Cave range from 17.9 to 20.7‰ VSMOW and are consistent with those from the higher resolution  $\delta^{18}\text{O}$  record (Lachniet et al., 2014). The  $\Delta^{17}\text{O}(\text{O}_2/\text{CaCO}_3)$  data range from -87 to -68 per meg. The data show a moderate negative trend when plotted in  $\Delta^{17}\text{O}$  vs.  $\delta^{18}\text{O}$  space (slope of -3.56 per meg/‰,  $r^2 = 0.42$ ) and are inconsistent with a single isotope forcing from cave kinetics ( $p < 0.01$ ) or from Rayleigh distillation (0 per meg/‰;  $p = 0.04$ ) (Fig. 6b).

The  $\delta^{18}\text{O}(\text{CO}_2/\text{CaCO}_3)$  data from Lehman Caves sample LMC-12b range from 21.0 to 25.6‰ VSMOW and are consistent with those from the higher resolution  $\delta^{18}\text{O}$  record. The  $\Delta^{17}\text{O}(\text{O}_2/\text{CaCO}_3)$  data range from -94 to -78 per meg. The data show a negative trend when plotted in  $\Delta^{17}\text{O}$  vs.  $\delta^{18}\text{O}$  space (slope of -3.17,  $r^2$  per meg/‰ = 0.70) and are inconsistent with a single isotope forcing from cave kinetics ( $p < 0.01$ ) or from Rayleigh distillation (0 per meg/‰;  $p = 0.02$ ) (Fig. 6c).

The  $\delta^{18}\text{O}(\text{CO}_2/\text{CaCO}_3)$  data from Lehman Caves sample WR-11 range from 18.5 to 20.1‰ VSMOW and are consistent with those from the higher resolution  $\delta^{18}\text{O}$  record (Steponaitis et al., 2015). The  $\Delta^{17}\text{O}(\text{O}_2/\text{CaCO}_3)$

Speleothem ID	$\Delta^{17}\text{O}$ vs. $\delta^{18}\text{O}$		$\Delta^{17}\text{O}$ vs. $\delta^{18}\text{O}$		$\Delta^{17}\text{O}$ vs. $\delta^{18}\text{O}$		$\Delta^{17}\text{O}$ vs. $\delta^{18}\text{O}$	$\Delta^{17}\text{O}$ vs. $\delta^{18}\text{O}$
	Slope (per meg/‰)	$r^2$	Slope 1 SE (per meg/‰)	$r^2$	$p$ for test-slope = +7 per meg/‰ <sup>1</sup>	$p$ for test-slope = 0 per meg/‰ <sup>1</sup>	$p$ for test-slope = -2 per meg/‰ <sup>1</sup>	
COB-01-02	-0.79	0.01	2.67	0.027	0.778	0.665	0.665	
LC-1	-3.56	0.42	1.46	9.14E-05	0.041	0.318	0.318	
LMC-12b	-3.18	0.70	0.93	1.11E-04	0.019	0.261	0.261	
WR-11	-3.94	0.39	2.49	0.012	0.188	0.479	0.479	
LMC-12b and LC-1	-3.36	0.82	0.40	8.17E-14	5.25E-07	0.004	0.004	
Water data set					<b>Slope 1 SE</b> (‰/‰)	<b>Slope 1 SE</b> (‰/‰)	<b><math>r^2</math></b>	
modern meteoric water	-3.57	0.58	0.58	0.69	0.5244	0.0006	0.99998	
formation water (COB and LC) <sup>2</sup>	-3.23	0.58	0.36	0.66	0.5248	0.0006	0.99998	
formation water (all samples)	-3.12	0.72	0.72	0.72	0.5249	0.0004	0.99999	

<sup>1</sup>  $p$  Values are calculated against test-slopes for cave kinetic, Rayleigh-style, and evaporation/seasonality processes (+7, 0, and -2, respectively).

<sup>2</sup> Only includes samples from Cave of the Bells and Leviathan Cave (see Sections 5.3 Reconstructed formation water isotope composition and 6 Discussion).

Table 3  
Summary statistics for trends in triple oxygen isotope data.

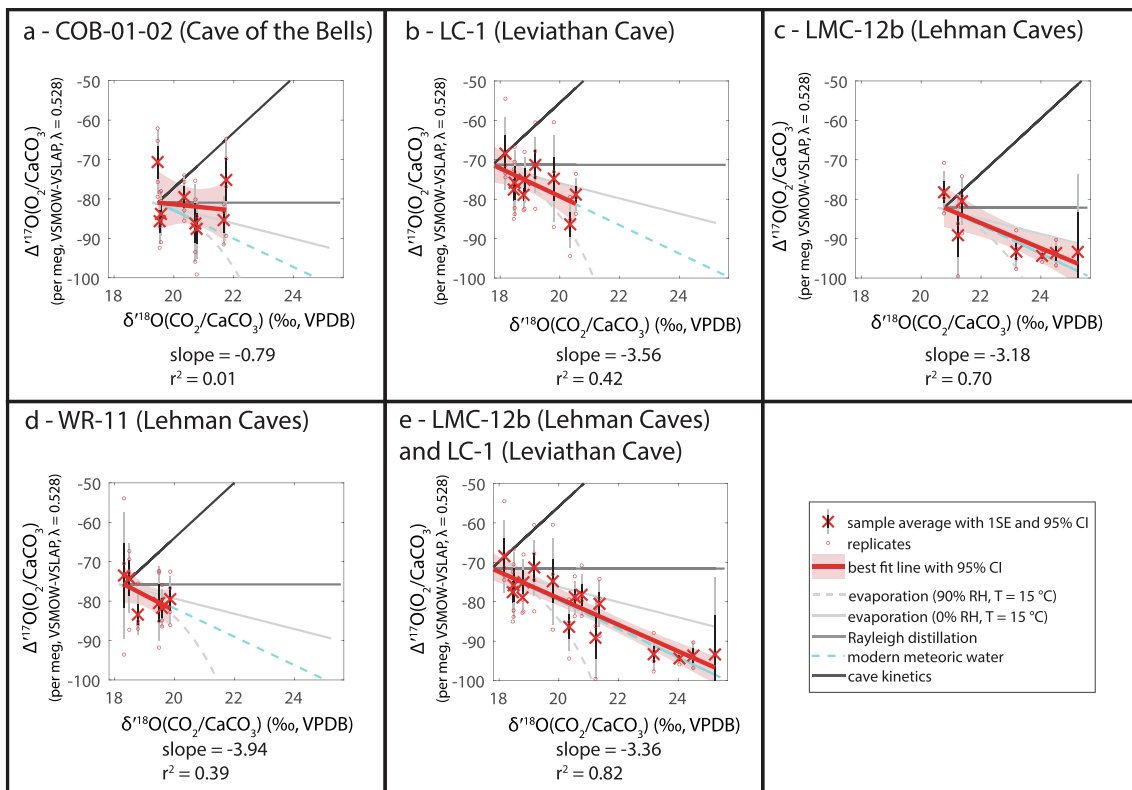


Fig. 6. Data in  $\Delta^{17}\text{O}(\text{O}_2/\text{CaCO}_3)$  vs.  $\delta^{18}\text{O}(\text{CO}_2/\text{CaCO}_3)$  space and inferred trends. Each panel shows the data replicates (red dots), sample averages (red 'x's), and the data trend (thick red line with pink 95% confidence interval, 95% CI). (a) Data for Cave of the Bells sample COB-01-02. (b) Data for Leviathan Cave sample LC-1. (c) Data for Lehman Caves sample LMC-12b. (d) Data for Lehman Caves sample WR-11. (e) Data for Lehman Caves sample LMC-12b and Leviathan Cave sample LC-1. The 1 SE and 95% CIs for  $\Delta^{17}\text{O}$  data are shown by the black and gray vertical lines (if the sample has one replicate the external precision of carbonate standards is used instead). The 1σ error bars for  $\delta^{18}\text{O}(\text{CO}_2/\text{CaCO}_3)$  data are generally smaller than the symbols and not shown. Summary statistics for the trendline are below the data plot. All plots are on the same scale. Thin lines show characteristic trends for hydrologic processes. Light gray lines show pan (i.e., local) evaporation trends (<-2 per meg/‰) under low and high relative humidity (RH) conditions at a temperature (T) of 15 °C (solid line at 90% RH, dashed line at 0% RH) (Criss, 1999; Luz and Barkan, 2010; Passey and Ji, 2019). Note the non-linearity of the evaporation trend under high RH conditions. No lines shown for the moisture source or formation temperature trends as they are contained within bounds of the local evaporation lines. The cyan dashed line is the seasonality trend inferred for modern waters (slope = -3.6 per meg/‰; see also Figs. 2 and 7). The medium gray line shows the near-horizontal trend for Rayleigh distillation processes (shown as 0 per meg/‰) (Criss, 1999; Barkan and Luz, 2005). The dark gray line shows the positive trend expected for cave kinetic processes (+7 per meg/‰) (fast degassing and prior calcite precipitation) (Guo and Zhou, 2019a, 2019b). All lines are calculated as the deviation from the data trendline starting at the most negative  $\delta^{18}\text{O}_{\text{speleothem}}$  value. (For interpretation of the references to colour in this figure legend, the reader is referred to the web version of this article.)

data range from -83 to -73 per meg. The data show a moderate negative trend when plotted in  $\Delta^{17}\text{O}$  vs.  $\delta^{18}\text{O}$  space (slope of -3.94 per meg/‰,  $r^2 = 0.39$ ) and are inconsistent with a single isotope forcing from cave kinetics ( $p = 0.01$ ) (Fig. 6d).

The combined LMC-12b and LC-1 data set (Lehman and Leviathan caves) has  $\delta^{18}\text{O}(\text{CO}_2/\text{CaCO}_3)$  ranging from 17.9 to 25.6‰ VSMOW and  $\Delta^{17}\text{O}(\text{O}_2/\text{CaCO}_3)$  ranging from -94 to -68 per meg. The data exhibit a strong negative trend when plotted in  $\Delta^{17}\text{O}$  vs.  $\delta^{18}\text{O}$  space (slope of -3.36 per meg/‰,  $r^2 = 0.82$ ) (Fig. 6e). A similar trend emerges if the WR-11 data are included (slope of -3.18 per meg/‰,  $r^2 = 0.77$ ) or if only Holocene data from both caves are considered (slope of -3.01 per meg/‰,  $r^2 = 0.81$ ). The data are inconsistent with the cave kinetics trend ( $p = <0.01$ ) and the Rayleigh distillation trend ( $p < 0.01$ ).

### 5.3. Reconstructed formation water isotope composition

We primarily discuss reconstructed formation water isotopic composition for Cave of the Bells and Leviathan Cave (Fig. 7) as previous studies and our data support their formation in (near) equilibrium conditions and they are therefore most likely to represent regional-scale hydrologic processes (see 6 Discussion). However, all reconstructions are available in the Supplementary Material (Supplementary Material, Fig. S6, Table S3). The isotopic composition of formation waters for the Cave of the Bells and Leviathan Cave data overlap with the modern waters and show the same overall trend. For Cave of the Bells, reconstructed formation water  $\delta^{18}\text{O}$  ranges from -9.8 to -7.5‰ VSMOW-SLAP while  $\Delta^{17}\text{O}$  ranges from 0 to 17 per meg VSMOW-SLAP. For Leviathan Cave, reconstructed for-

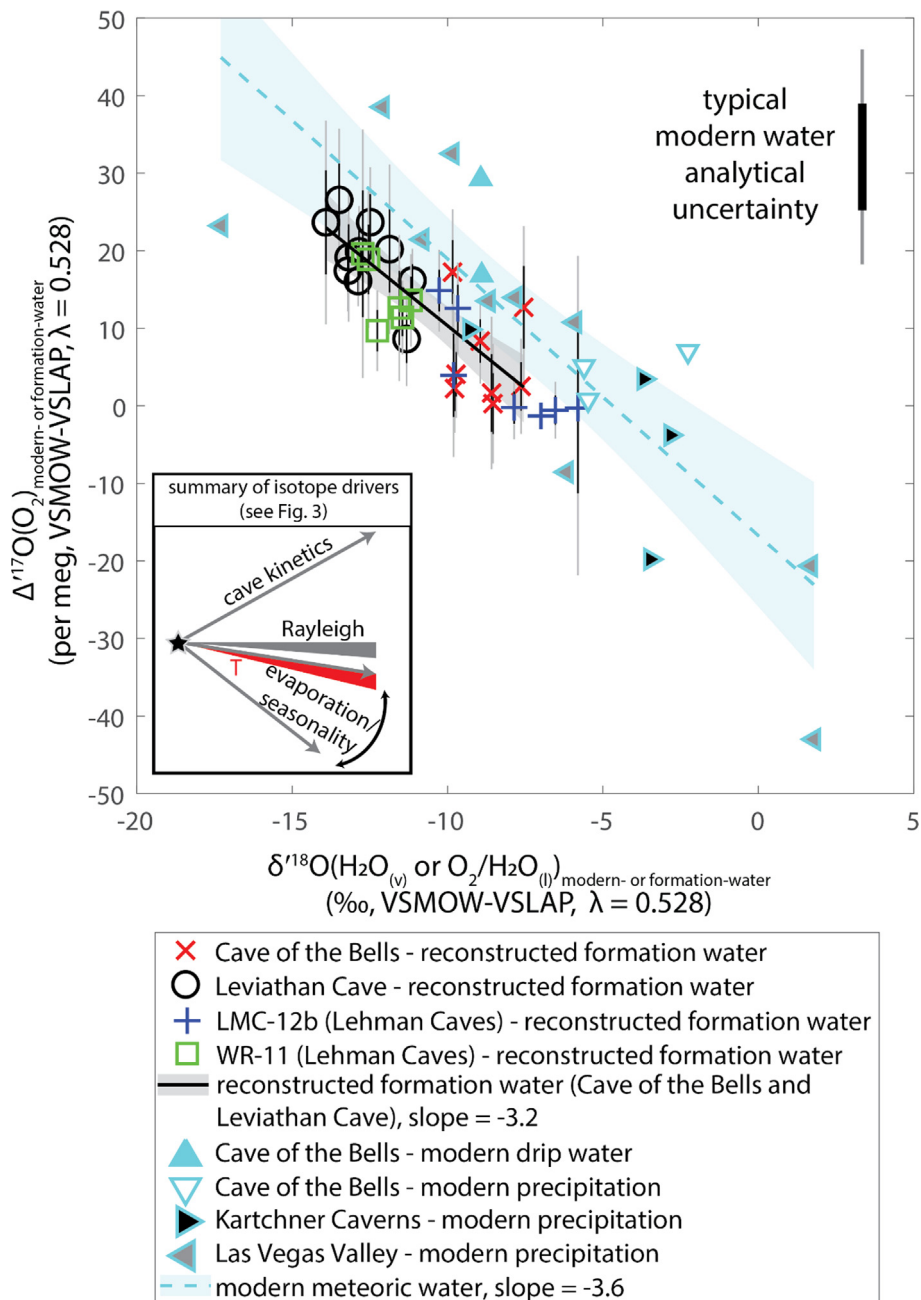


Fig. 7. Triple oxygen isotope results for modern Arizona and Nevada meteoric waters compared to reconstructed formation waters. Reconstructed formation waters, calculated from  $\delta^{18}\text{O}(\text{H}_2\text{O}_{(\text{v})}/\text{H}_2\text{O}_{(\text{l})})$  and  $\Delta^{17}\text{O}(\text{O}_2/\text{CaCO}_3)$ , for Cave of the Bells (COB) are red x's, for Leviathan Cave are black circles, for LMC-12b data (Lehman Caves) are blue crosses, and for WR-11 data (Lehman Caves) are green squares. Modern meteoric water data [ $\delta^{18}\text{O}(\text{H}_2\text{O}_{(\text{v})}/\text{H}_2\text{O}_{(\text{l})})$  and  $\Delta^{17}\text{O}(\text{O}_2/\text{H}_2\text{O})$ ] are the cyan triangles: Cave of the Bells drip waters are upward-pointing triangles with cyan fill, Cave of the Bells precipitation samples are downward-pointing triangles with white fill, Kartchner Caverns precipitation samples are right-pointing triangles with black fill, and Nevada precipitation samples are left-pointing triangles with gray fill. The ordinary least squares regression for reconstructed formation waters from Cave of the Bells and Leviathan Cave is the solid black line and for all modern meteoric waters is the dashed cyan line (with 95% confidence intervals shaded in gray and cyan, respectively; see Supplementary Material, Fig. S6 as well). The summary of triple oxygen isotope drivers relevant to speleothem triple oxygen isotopes in  $\Delta^{17}\text{O}$  vs.  $\delta^{18}\text{O}$  space (Fig. 3) is shown in the lower left inset). We calculated reconstructed water values using modern cave temperature, but uncertainty in this value for pre-Holocene data is unlikely to affect the broad-scale patterns of the data (see section 4.5 *Estimation of  $\theta_{\text{CaCO}_3-\text{H}_2\text{O}}$  and reconstructing formation water isotope composition* for details; Supplementary Material, Fig. S5). Analytical 1 SE and 95% confidence intervals for reconstructed water  $\Delta^{17}\text{O}$  are shown by the black and gray vertical lines, respectively (for clarity, these are not shown for modern waters, see Table 2; Supplementary Material, Table S2). Error for  $\delta^{18}\text{O}$  values is smaller than the symbols. (For interpretation of the references to colour in this figure legend, the reader is referred to the web version of this article.)

mation water  $\delta^{18}\text{O}$  ranges from  $-13.9$  to  $-11.1\text{\textperthousand}$  VSMOW-SLAP and  $\Delta^{17}\text{O}$  ranges from  $9$  to  $27$  per meg VSMOW-SLAP. Within the Leviathan Cave data set, Holocene and older samples are largely indistinguishable, suggesting that the isotopic trends are not affected by uncertainty in pre-Holocene cave temperatures (Cave of the Bells has no Holocene data). This is supported by the reconstructed formation water data trend of  $\Delta^{17}\text{O} = -3.2 \times \delta^{18}\text{O} - 22.0$  ( $r^2 = 0.66$ ), which is similar to the modern LMWL (see also potential data trends with variable formation temperatures; Supplementary Material, Fig. S5). The combined formation water data set has a  $\delta^{17}\text{O}$  vs.  $\delta^{18}\text{O}$  slope of  $0.5249$ , or, if only Cave of the Bells and Leviathan Cave data are considered, of  $0.5248$ .

#### 5.4. Triple oxygen isotope trends through time

Although our drilling resolution is coarse and samples largely overlap only on the broadest (1–10 s kyr) timescales, several trends are apparent in  $\Delta^{17}\text{O}_{\text{speleothem}}$  through time (Fig. 8). The LMC-12b and WR-11 records both show “fishhook” shaped patterns with minima early in the record, increases to maxima in the middle, and a final decrease towards the end of the record. While the patterns are similar in shape, they occur at different times. The pattern visible in LMC-12b occurs over 16–6 ka, with the minimum at 9 ka while the pattern of WR-11 occurs over 11–4 ka, with the minimum at 7 ka (although note that WR-11 data variability is likely at the limit of what is analytically resolvable).

Over longer timescales, Cave of the Bells and Leviathan Cave largely show distinct  $\Delta^{17}\text{O}_{\text{speleothem}}$  values. Leviathan Cave  $\Delta^{17}\text{O}_{\text{speleothem}}$  averages  $-76 \pm 5$  per meg VSMOW-SLAP over 100–0 ka, while Cave of the Bells  $\Delta^{17}\text{O}_{\text{speleothem}}$

averages  $-82 \pm 5$  per meg VSMOW-SLAP over 50–20 ka. Leviathan Cave data are invariant except potentially in the oldest sample at 101 ka, which is 5–10 per meg lower than other data. Cave of the Bells data has a hump-shaped profile from 50–38 ka followed by a return to a more positive value at 20 ka.

## 6. DISCUSSION

### 6.1. Inferred drivers of speleothem triple oxygen isotope variability

Except for sample WR-11 data, the triple oxygen isotope data from this study support our predictions about the possible trends for speleothem isotope composition given prior interpretations. The near-horizontal trend outlined by the Cave of the Bells data (COB-01-02) in  $\Delta^{17}\text{O}$  vs.  $\delta^{18}\text{O}$  space supports prior interpretations of  $\delta^{18}\text{O}_{\text{speleothem}}$  variability as the result of Rayleigh distillation (precipitation amount, frequency of extreme precipitation events) and relatively small variations in the temperature of mineralization ( $<10$  °C) that cause  $\Delta^{17}\text{O}$  variability within our analytical precision (Fig. 6a) (Wagner et al., 2010; Eastoe and Dettman, 2016). Because modern water data show that the seasonal precipitation trend is negative in triple oxygen isotope space (Figs. 2f, 7; Tables 2 and 3), the data suggest changes in seasonality of precipitation/infiltration or evaporation are unlikely to have driven variability in  $\delta^{18}\text{O}_{\text{speleothem}}$ . Similarly, the moderate negative trend outlined by the Leviathan Cave data (LC-1) supports prior interpretations of  $\delta^{18}\text{O}_{\text{speleothem}}$  resulting from variation in Rayleigh distillation, mineralization temperature, and moisture source (Fig. 6b) (Lachniet et al., 2014; Lachniet et al., 2017; Lachniet et al., 2020).

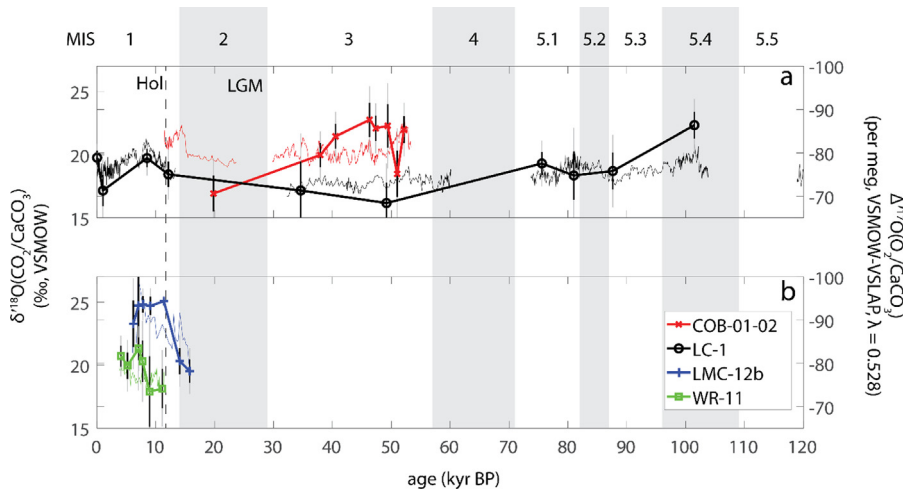


Fig. 8. Speleothem triple oxygen isotope data through time. In both panels, thin colored lines are higher resolution  $\delta^{18}\text{O}(\text{CO}_2/\text{CaCO}_3)$  data from the original publications (left axes, converted to VSMOW), while bold lines and large symbols are  $\Delta^{17}\text{O}(\text{O}_2/\text{CaCO}_3)$  data (right axis, note axes are inverted). In (a), data for Cave of the Bells (COB-01-02) are red x's and for Leviathan Cave (LC-1) are black circles. In (b) data for Lehman Caves samples LMC-12b and WR-11 are shown in blue crosses and green squares, respectively. The 1 SE and 95% confidence intervals for  $\Delta^{17}\text{O}$  data are shown by the black and gray vertical lines (if the sample has one replicate the external precision of carbonate standards is used instead). Marine Isotope Stages (MIS, gray and white bands) are labeled above panel (a) (LR04 benthic stack; Lisiecki and Raymo, 2005), the approximate time of the Last Glacial Maximum is marked at 20–25 ka (LGM), and the start of the Holocene (Hol) is marked at 11.7 ka (dashed line). (For interpretation of the references to colour in this figure legend, the reader is referred to the web version of this article.)

Samples from Lehman Caves delineate moderate-to-strong negative trends in  $\Delta'^{17}\text{O}$  vs.  $\delta'^{18}\text{O}$  space, supporting evaporative or seasonality-related processes as important drivers of  $\delta^{18}\text{O}_{\text{speleothem}}$  variability (Fig. 6c–d). Given the strength of these trends, it is reasonable to expect that these samples were also influenced by Rayleigh-style processes that “smeared” the evaporation signal. As Lehman Caves samples are largely Holocene in age, variability in the temperature of mineral formation likely had only a small effect on sample isotope composition (temperature sensitivity of 1 °C causes a  $\approx 0.25\text{\textperthousand}$  change in  $\delta^{18}\text{O}$  and  $\approx 1$  per meg in  $\Delta'^{17}\text{O}$ ; Kim and O’Neil, 1997; Madsen et al., 2001; Coplen, 2007; Reinemann et al., 2009; Cao and Liu, 2011; Harbert and Nixon, 2018; Hayles et al., 2018; Guo and Zhou, 2019b; Wostbrock et al., 2020a; Schauble and Young, 2021).

The  $\Delta'^{17}\text{O}$  vs.  $\delta'^{18}\text{O}$  trend of sample LMC-12b supports our predictions and is even stronger when considered in the context of the Leviathan Cave record (Fig. 6e). The same trend emerges regardless of whether pre-Holocene data (largely from LC-1) are excluded. The broader view from the combined data set emphasizes the local processes acting on speleothem isotope composition because these caves would have received precipitation with a common history (the caves are only 180 km apart). There are two potential explanations for the negative data trend: changes in precipitation or infiltration seasonality, and variable evaporation during infiltration (e.g., in the soil or deeper subsurface). Changes in precipitation or infiltration seasonality cannot explain the data alone because the most negative  $\Delta'^{17}\text{O}$  values (and most positive  $\delta'^{18}\text{O}$  values) would require the speleothem to be primarily recording summer rainfall (Fig. 7; Table 2; Supplementary Material, Tables S2 and S3). This is unlikely because of the strong winter-water bias of groundwater recharge in Nevada (i.e., this location has regular winter snowpack; Winograd et al., 1998), which makes it difficult to imagine a scenario where only summer infiltration would influence speleothem growth. In turn, if local evaporation was the only driver, given the  $\delta'^{18}\text{O}$  range of the data and the likely high relative humidity conditions of subsurface evaporation, curvature might be visible in the data trend (see the characteristic trend for evaporation at 90% relative humidity; Fig. 6e). The additional information provided by  $\Delta'^{17}\text{O}$  data therefore allows us to infer that a combination of local seasonality and evaporation effects is the most likely explanation for the data, which would not be evident from  $\delta'^{18}\text{O}$  data alone.

Sample WR-11 shows a negative trend in  $\Delta'^{17}\text{O}$  vs.  $\delta'^{18}\text{O}$  space, the opposite of our predicted cave kinetic trend based on prior  $\delta^{18}\text{O}$ ,  $\delta^{13}\text{C}$ , and Mg/Ca results and the theoretical cave kinetics trend for triple oxygen isotopes (Fig. 6d) (Steponaitis et al., 2015; Guo and Zhou, 2019a). It is possible that our data contradict prior interpretations by Steponaitis et al. (2015), but we are also cognizant of deficiencies in this data set. Our coarse sampling resolution may have missed the most affected time periods and more detailed sampling might show that the magnitude of cave kinetic effects varied in importance through time. More critically, we were not able to acquire the entire available  $\delta'^{18}\text{O}$  range for this sample (available range of 2.6‰ vs. sampled

range of 1.5‰). This may preclude rigorous identification of the actual signal (Supplementary Material, Fig. S1). Alternatively, it is possible that modeling of triple oxygen isotope deviations due to cave kinetic effects insufficiently represents real systems (Guo and Zhou, 2019a; Guo and Zhou, 2019b). It will be important to verify this modeling work through analyses of natural and synthetic calcites and speleothems grown under near-equilibrium and kinetic conditions (e.g., Mickler et al., 2004; Mickler et al., 2006; Banner et al., 2007; Day and Henderson, 2011; Hansen et al., 2019; Mickler et al., 2019; EL-Shenawy et al., 2020). Regardless of the cause, this result emphasizes the utility of having several lines of evidence in interpreting speleothem isotope composition as well as the importance of sampling design in interpreting  $\Delta'^{17}\text{O}$  data.

## 6.2. Triple oxygen isotope trends through time

While we have largely focused on data trends apparent in  $\Delta'^{17}\text{O}$  vs.  $\delta'^{18}\text{O}$  space as a test of the triple oxygen isotope geochemical framework, there are also trends in  $\Delta'^{17}\text{O}$  through time (Fig. 8). We discuss patterns in carbonate data here but note that the same patterns are apparent in the reconstructed water values (Supplementary Material, Fig. S7). The fishhook-shaped pattern exhibited by Lehman Caves data may correspond with known paleoclimate events in the western USA. For example, many western USA records show prominent warming and/or drying conditions in the early to mid-Holocene (e.g., the compilations in Steponaitis et al., 2015; Schuman and Serravezza, 2017; Lachniet et al., 2020). While decreased  $\Delta'^{17}\text{O}$  from increased local evaporation in both Lehman Caves records is consistent with this paleoclimate background, the difference in when the minima occurs suggests that variable precipitation or infiltration seasonality and infiltration routes are also important.

The differences between Cave of the Bells and Leviathan Cave  $\Delta'^{17}\text{O}$  data through time may speak to broader-scale climate features. We consider our data in the context of  $\Delta'^{17}\text{O}$  of modern tap and river water from the western USA (west of 100° W), which increases with latitude (Li et al., 2015; Bershad et al., 2020). The exact role of moisture source region conditions (e.g., relative humidity, turbulence), moisture recycling, vapor mixing, and smaller-scale processes (e.g., rainfall re-evaporation) in controlling tap water  $\Delta'^{17}\text{O}$  is not yet clear, in part due to the paucity of data. However, it is promising that our modern water and 50–38 ka speleothem data from Cave of the Bells and Leviathan Cave both show the same latitudinal gradient in  $\Delta'^{17}\text{O}$  values as the tap water data set, with  $\Delta'^{17}\text{O}$  increasing northward. Intriguingly, this gradient may change through time, as indicated by the U-shaped Cave of the Bells data, and may even reverse (see the Cave of the Bells data point at 20 ka). If this change in gradient is real, it suggests that  $\Delta'^{17}\text{O}$  data are recording information about the dramatic hydrologic changes taking place during the transitions into and out of the LGM. There is evidence that  $\Delta'^{17}\text{O}$  of water encodes information about the conditions of the regional moisture source during evaporation (Barkan and Luz, 2007; Uemura et al., 2010; Uechi and Uemura, 2019)

and we recognize attempts to reconstruct, for example, relative humidity (normalized to sea surface conditions) from carbonate speleothems (Sha et al., 2020). However, at our continental interior sites, as Li et al. (2015) note, there are several other parameters that may be expected to vary through time and it is not yet feasible to parse out the relative importance of these factors in modern, much less ancient, datasets of the western USA. We accordingly conclude that  $\Delta^{17}\text{O}_{\text{Speleothem}}$  data along the gradient defined by Cave of the Bells and Leviathan Cave is likely recording regional-scale evidence of Quaternary hydrologic change, but are unable to specify the exact mechanisms responsible.

### 6.3. Inferences from formation water triple oxygen isotope composition

We have thus far discussed trends in carbonate data but recognize that interpretations of formation water values would be more robust if carbonate formation temperatures were well-constrained. Except for Holocene-aged samples, we do not have precise constraints on formation temperature. However, consideration of a wide array of potential formation temperatures demonstrates that reconstructed water data support, and emphasize, the trends interpreted from carbonate data. (SI Text and Supplementary Material, Fig S5). In addition to the data trends, there are clear connections between modern and reconstructed waters. Our triple oxygen isotope data identify Cave of the Bells

and Leviathan Cave samples as reflective of changes in regional precipitation, and it is promising that their inferred formation water isotope values match that of measured precipitation and drip water (Fig. 7; Supplementary Material, Fig. S6). This provides additional support for the utility and fidelity of paleoclimate reconstructions from these locations. The reconstructed water values are also within the range of modern waters from the western USA (Figs. 7 and 9) (Li et al., 2015; Bershad et al., 2020; Aron et al. 2021). In addition, these reconstructed formation waters exhibit similar trends our LMWL: slopes for  $\Delta^{17}\text{O}$  vs.  $\delta^{18}\text{O}$  are  $-3.2$  and  $-3.6$  per meg/‰, respectively, and for  $\delta^{17}\text{O}$  vs.  $\delta^{18}\text{O}$  are  $0.5248$  and  $0.5244$ , respectively (Table 3). While we infer that the reconstructed formation water values from Lehman Caves likely fall on a similar trend to modern waters because local evaporation and seasonality effects cause negative trends similar to far-field moisture source effects (Supplementary Material, Fig. S6, Table S3), their inclusion in the data set does not significantly change the trend (all data produces a  $\Delta^{17}\text{O}$  vs.  $\delta^{18}\text{O}$  slope of  $-3.1$  per meg/‰ and a  $\delta^{17}\text{O}$  vs.  $\delta^{18}\text{O}$  slope of  $0.5249$ ; Table 3).

The patterns in our data lead to two broad conclusions related to assessing the importance of cave kinetic effects in single speleothem-based paleoclimate reconstructions. First, all the observed triple oxygen isotope trends are likely distinguishable from the theoretical cave kinetics trend, which is strong evidence that variation in the triple oxygen isotope composition of reconstructed formation waters

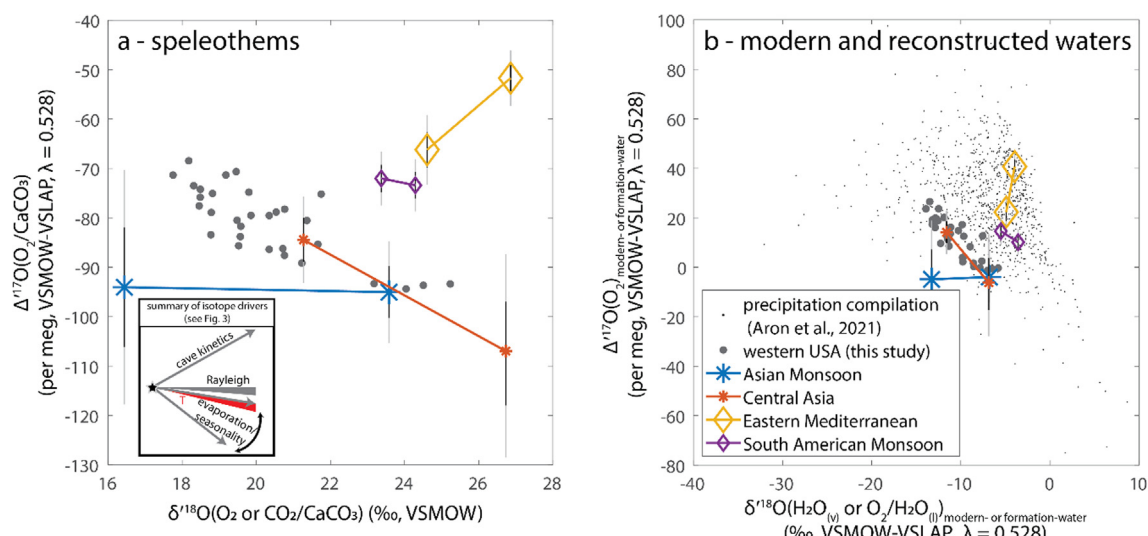


Fig. 9. Data comparison with that of Sha et al. (2020) and global modern waters. (a) Comparison of speleothem data in  $\Delta^{17}\text{O}(\text{O}_2/\text{CaCO}_3)$  vs.  $\delta^{18}\text{O}(\text{O}_2 \text{ or } \text{CO}_2/\text{CaCO}_3)$  space. Data from this study are dark gray circles and Sha et al. (2020) data, organized by region, are the colored stars and diamonds (large blue stars, Asian Monsoon; small orange stars, central Asia; large yellow diamonds, Eastern Mediterranean; small purple diamonds, South American Monsoon). Lines connecting the two-point datasets for each region explored by Sha et al. (2020) show the preliminary trends we interpret in the context of our geochemical framework (lower left inset, see also Fig. 3). (b) Modern and reconstructed formation water data in  $\Delta^{17}\text{O}(\text{O}_2/\text{CaCO}_3)$  vs.  $\delta^{18}\text{O}(\text{H}_2\text{O}_{(v)} \text{ or } \text{O}_2/\text{H}_2\text{O}_{(l)})$  space. The color scheme follows panel (a), but all data are plotted over the globally distributed modern precipitation compilation of Aron et al. (2021) (light gray dots). Note that, consistent with treatment of our own data, we renormalized Sha et al. (2020) data to the  $\Delta^{17}\text{O}$  mineral values of carbonate standards reported by Wostbrook et al. (2020b) (Supplementary Material text; Supplementary Material, Tables S7 and S8). Analytical 1 SE and 95% confidence intervals for  $\Delta^{17}\text{O}$  of Sha et al. (2020) data are shown by the black and gray vertical lines, respectively [for clarity, these are not shown for data from this study and Aron et al. (2021)]. Error for  $\delta^{18}\text{O}$  values is smaller than the symbols. (For interpretation of the references to colour in this figure legend, the reader is referred to the web version of this article.)

through time is, within error limits, due largely to climate-related processes. Our data therefore provide an additional line of evidence that supports western USA  $\delta^{18}\text{O}_{\text{speleothem}}$  as responding to climate-driven signals related to air mass and precipitation Rayleigh distillation, atmospheric precipitation and infiltration seasonality, and moisture source conditions, alongside variability in mineralization temperature.

Second, reconstructed water values plot near the modern LMWL, which suggests that, within error limits, the absolute values of reconstructed waters are representative of drip water values. If samples had a significant offset due to cave kinetics, data would plot above the modern LMWL (Guo and Zhou, 2019a; Fig. 2e). This result is most robust for Holocene-aged samples for which the formation temperature is best constrained. Note, however, that choice of  $\alpha^{18}\text{CaCO}_3-\text{H}_2\text{O}$  and, specifically,  $\theta_{\text{CaCO}_3-\text{H}_2\text{O}}$  are important in this determination. Using values from Wostbrock et al. (2020a) ( $\theta_{\text{CaCO}_3-\text{H}_2\text{O}} = 0.5254\text{--}0.5260$ ; 5–35 °C) would move  $\Delta^{17}\text{O}$  values 10–30 per meg below the LMWL, those of Bergel et al., 2020 ( $\theta_{\text{CaCO}_3-\text{H}_2\text{O}} = 0.5246\text{--}0.5253$ ; 15–28 °C) would move  $\Delta^{17}\text{O}$  values closer to the LMWL (values increase by ≈5 per meg), and those of Voarintsoa et al., 2020 ( $\theta_{\text{CaCO}_3-\text{H}_2\text{O}} = 0.5234\text{--}0.5242$ ; 10–35 °C) would move  $\Delta^{17}\text{O}$  values ≈30 per meg above the LMWL.

We conclude that two metrics can be obtained from  $\Delta^{17}\text{O}$  vs.  $\delta^{18}\text{O}$  data, comparing (1) trends within individual reconstructed formation water isotope datasets against the theoretical cave kinetics trend and (2) the absolute values of reconstructed formation water isotope composition against a site's LMWL. Testing for absolute differences will be more feasible in older samples if there are independent constraints on ancient LMWLs (e.g., via groundwater or speleothem fluid inclusion isotope composition) and speleothem formation temperatures (see overview of Meckler et al. 2021). More precise determinations of  $\theta_{\text{CaCO}_3-\text{H}_2\text{O}}$  will also be critical for this endeavor (Sharp and Wostbrock, 2021). Regardless, our proposed metrics will serve as new ways to assess the importance of cave kinetic processes in  $\delta^{18}\text{O}$  speleothem record interpretation (Fig. 7) (e.g., Hendy, 1971).

#### 6.4. Comparison to and additional interpretations of Sha et al. (2020) data

In addition to guiding interpretations at our study site, our proposed geochemical framework also adds context to the data of Sha et al. (2020), the only other study of triple oxygen isotope data in carbonate speleothems. Sha et al. (2020) analyzed pairs of speleothem samples for triple oxygen isotopes within the climate regimes of the Asian monsoon (Jiangjun Cave, Yunnan, China), South American monsoon (El Condor cave, northern Peru), Westerlies (Tonnel'naya Cave, Uzbekistan), and Mediterranean (Jeita Cave, northern Levant). After renormalizing their data to the Wostbrock et al. (2021) mineral values (Supplementary Material text, Tables S7 and S8), the Sha et al. (2020) carbonate  $\Delta^{17}\text{O}$  values cover a slightly wider range (−107 to −52 per meg) than our own (−94 to −68 per meg) (Fig. 9a). However, much of the discrepancy in carbonate  $\Delta^{17}\text{O}$  ranges comes from differences in formation tempera-

ture, as can be seen in the better overlap of reconstructed formation water  $\Delta^{17}\text{O}$  values [−6 to 41 per meg for Sha et al. (2020) and −1 to 27 per meg for this study] (Fig. 9b). It is also encouraging that both studies have reconstructed formation water  $\Delta^{17}\text{O}$  values within the observed range of modern precipitation  $\Delta^{17}\text{O}$  values (Aron et al., 2021).

In interpreting data trends, we are constrained by analytical precision and by individual data sets each containing only two points. We therefore only interpret data sets with wide  $\delta^{18}\text{O}$  or  $\Delta^{17}\text{O}$  ranges (>5‰ and/or >10 per meg ranges, respectively) to identify likely trends, and exclude El Condor cave from discussion.

The Jiangjun Cave data show a nearly horizontal trend (0.1 per meg/‰), the Tonnel'naya Cave data show a negative trend (−4.3 per meg/‰), and the Jeita Cave data show a strong positive trend (19.4 per meg/‰). The Jiangjun Cave trend is consistent with Rayleigh distillation as an important driver of speleothem  $\delta^{18}\text{O}$ . This is supported by modern precipitation data from Singapore, also within the Asian monsoon region, that show a near-horizontal trend with minimal correlation in  $\Delta^{17}\text{O}$  vs.  $\delta^{18}\text{O}$  space (−0.9 per meg/‰ with  $r^2 = 0.03$ ; Fig. 2f; He et al., 2021). Note, however, that more ambiguous situations can exist, as this seasonal pattern may not be widespread across the region. For example, modern precipitation data from Okinawa Island, Japan show a positive relationship in  $\Delta^{17}\text{O}$  vs.  $\delta^{18}\text{O}$  space (+2.9 per meg/‰; Fig. 2f; Uechi and Uemura, 2019). It is therefore possible that precipitation seasonality in this region may exhibit horizontal to positive trends in  $\Delta^{17}\text{O}$  vs.  $\delta^{18}\text{O}$  space. Where precipitation seasonality and cave kinetics trends have similarly positive slopes, they cannot be distinguished with triple oxygen isotope data alone. Regardless, a minimal role for variation in cave kinetic processes at Jiangjun Cave is supported both by the preliminary triple oxygen isotope trend and by considering prior assessments of limited variability in cave kinetics (e.g., replication of signal within or between cave sites; Dorale and Liu, 2009; and as applied to sites in this region, e.g., Wang et al., 2001; Yin et al., 2014; Liang et al., 2020). Given this evidence, the Jiangjun Cave data are likely consistent with previous interpretations of speleothem  $\delta^{18}\text{O}$  from the Asian monsoon region as influenced by changing proportions of monsoon rainfall (Wang et al., 2001; Cheng et al., 2009) and continental-scale rainout from Pacific and Indian Ocean moisture sources (Yuan et al., 2004; Pausata et al. 2011) in addition to any effect from variable formation temperature.

The negative trend for the Tonnel'naya Cave data is consistent with variable evaporation conditions, precipitation or infiltration seasonality, and formation temperature as the strongest drivers of speleothem  $\delta^{18}\text{O}$ . These factors are consistent with previous interpretations of speleothem  $\delta^{18}\text{O}$  variation resulting from large-scale changes to atmospheric circulation (rainfall amount, temperature, seasonality, moisture source, and moisture trajectories) as well as local temperature (Cheng et al., 2016).

Finally, the strong positive trend for the Jeita Cave data is most consistent with variable cave kinetic processes as a primary driver of speleothem  $\delta^{18}\text{O}$ . However, as in the

Asian monsoon region, it is important to consider variability in the trend of precipitation seasonality. If, unlike at present (Cheng et al., 2015), ancient climate in the eastern Mediterranean was significantly influenced by a northward-expanded African summer monsoon (e.g., Orland et al., 2019), Jeita Cave precipitation seasonality may have had a positive trend similar to some portions of the modern Asian Monsoon region (Uechi and Uemura, 2019, Fig. 2f).

The sum of these interpretations, even considering the inherent difficulty of identifying trends from two-point datasets, is that there is likely significant variability in the trends observed in  $\Delta^{17}\text{O}$  vs.  $\delta^{18}\text{O}$  space that may be reasonably expected from prior climate-based interpretations of  $\delta^{18}\text{O}_{\text{speleothem}}$ . In some cases, as at Jeita Cave, interpretations based solely on triple oxygen isotopes raise the possibility of cave kinetic influence. However, where outside data suggest significant cave kinetic influence through time is unlikely (e.g., via inter-cave replication tests), seasonal and spatial variability in precipitation triple oxygen isotopes is a more likely cause.

## 7. CONCLUSIONS AND OUTLOOK FOR USING TRIPLE OXYGEN ISOTOPES IN SPELEOTHEM PALEOCLIMATOLOGY

This study partially demonstrates the validity of a geochemical framework for applying triple oxygen isotopes in speleothem paleoclimatology and adds to a growing number of related studies (Affolter et al., 2015; Gásquez et al., 2017, 2020; Sha et al., 2020). The identification of key patterns in the triple oxygen isotope framework (Fig. 3) shows that  $\Delta^{17}\text{O}$  vs.  $\delta^{18}\text{O}$  data has an important role in speleothem paleoclimatology. With relevance to western USA paleoclimatology, it is particularly notable that the reconstructed formation waters from samples covering Nevada and Arizona show a similar trend to this study's LMWL, supporting prior interpretations of isotopic variability as strongly tied to climate drivers and not cave kinetic processes. More broadly, data from other continents can potentially be explained within the proposed framework (Sha et al., 2020) and should be tested with more expansive datasets. In addition, our proposed tests for the absolute magnitude of cave kinetic effects (i.e., the offset from expected equilibrium values) and their temporal variability have immediate application for establishing the fidelity of  $\delta^{18}\text{O}_{\text{speleothem}}$  records as paleoclimate archives (Figs. 6 and 7) and may provide a basis for finding samples suitable for clumped isotope analysis (e.g., Affek et al., 2008; Daéron et al., 2011; Wainer et al., 2011; Kulge and Affek, 2012; Affek et al., 2014; Affek and Zaarur, 2014).

For the moment, triple oxygen isotope studies must rely on a relatively small number of  $\Delta^{17}\text{O}$  samples, given the 2.5-hr analysis time, and incorporate as wide a  $\delta^{18}\text{O}$  signal as possible ( $\geq 5\text{\textperthousand}$ ) to accommodate the  $\approx 10$  per meg analytical precision of  $\Delta^{17}\text{O}$  analyses. As shown here, triple oxygen isotope data of modern meteoric water and coarse-resolution speleothem triple oxygen isotope composition should form one basis for interpreting broad-scale patterns in high resolution  $\delta^{18}\text{O}_{\text{speleothem}}$  records (e.g., in concert

with speleothem trace element and  $\delta^{13}\text{C}$  records and records from other paleoclimate archives). In addition, studies might target specific intervals to investigate triple oxygen isotope drivers on sub-millennial time scales. Alternatively, studies could acquire expanded  $\delta^{18}\text{O}$  ranges, with correspondingly suitable  $\Delta^{17}\text{O}$  ranges, by combining speleothems from multiple sites with similar climatology (following, e.g., Bowen and Revenaugh, 2003; Liu et al., 2010; Kukla et al., 2019). Our Cave of the Bells and Leviathan Cave data provide an example of such a situation. By investigating speleothem records from the western USA along a latitudinal gradient, it would be possible to investigate a  $\delta^{18}\text{O}$  gradient of 5–10‰ (e.g., Asmerom et al., 2007, 2010; 2013; Denniston et al., 2007; Wagner et al., 2010; Lundeen et al., 2013; Lachniet et al., 2014; Steponaitis et al., 2015; Lachniet et al., 2017; Polyak et al., 2017; Lachniet et al., 2020). These data might inform hypotheses about spatial variability in the winter storm track (as tied to the conditions of evaporation at the moisture source) (e.g., Oster et al., 2015; Hudson et al., 2019), the degree of moisture recycling along hydrologic flowpaths, mixing of water sources (as vapor or in terms of infiltration seasonality), and precipitation style (Aron et al., 2021). This kind of experimental setup presents opportunities to increase the reliability and specificity of high-resolution  $\delta^{18}\text{O}_{\text{speleothem}}$  interpretations and create robust, multi-record paleoclimate syntheses that can inform proxy-climate model comparisons of ancient hydrologic processes (e.g., Braconnot et al., 2011; Braconnot et al., 2012; Oster et al., 2015; Hudson et al., 2019; Tierney et al., 2020).

However, triple oxygen isotope-based paleoclimate interpretations must be predicated on a more robust understanding of modern  $\Delta^{17}\text{O}$  systematics. Basic parts of the geochemical framework, like the theorized response of  $\Delta^{17}\text{O}$  to cave kinetic processes, still require experimental validation (Guo and Zhou, 2019a; Guo and Zhou, 2019b). The proposed weak temperature sensitivity of  $\Delta^{17}\text{O}$  to various fractionating processes needs further characterization, although several studies have now approached this problem (Barkan and Luz, 2007; Passey et al., 2014; Bergel et al. 2020; Sha et al., 2020; Voarintsoa et al., 2020; Wostbrock et al., 2020a). Long-term, regional- to global-scale data sets of  $\Delta^{17}\text{O}$  in vapor and precipitation, like those developed for  $\delta^{18}\text{O}$  and  $\delta\text{D}$  (Dansgaard, 1964; Bowen and Revenaugh, 2003), will be required to demonstrate hydrologic controls [see Aron et al. (2021) for a recent review and compilation of  $\Delta^{17}\text{O}$  data]. For example, several studies have worked to relate  $\Delta^{17}\text{O}$  data to source region relative humidity normalized to sea surface conditions (Barkan and Luz, 2007; Uemura et al., 2010; Uechi and Uemura, 2019; Sha et al., 2020). The data for maps of this “normalized relative humidity” already exist in climate reanalysis products and in climate model outputs (atmospheric humidity, air temperature, and sea surface temperature) and will be critical in developing a community understanding of the parameter: what is the expected range of values and how does it vary geographically and temporally in connection to  $\Delta^{17}\text{O}_{\text{precipitation}}$  (Risi et al., 2010; Risi et al., 2013; Schoenemann and Steig, 2016)? In turn, such data, through studies like this one, will be critical in

demonstrating how  $\Delta^{17}\text{O}_{\text{precipitation}}$  relates to  $\Delta^{17}\text{O}_{\text{speleothem}}$ . Ultimately, developing fundamental expectations for how hydrologic and geologic processes affect  $\Delta^{17}\text{O}_{\text{speleothem}}$  will allow speleothem paleoclimatologists to identify appropriate study sites for investigating  $\Delta^{17}\text{O}$ -based hypotheses and produce more accurate, bounded reconstructions of ancient hydrologic processes from  $\Delta^{17}\text{O}_{\text{speleothem}}$  analyses (e.g., as has been demonstrated for lake deposits by Passey and Ji, 2019).

## Declaration of Competing Interest

The authors declare that they have no known competing financial interests or personal relationships that could have appeared to influence the work reported in this paper.

## ACKNOWLEDGEMENTS

The authors thank Drake Yarian, Phoebe Aron, Julia Kelson, Natalie Packard, Sarah Katz, Elise Pelletier, and Nicholas Ellis for assistance with the  $\Delta^{17}\text{O}$  analyses, Lora Wingate and Kelsey Dyez for assistance with  $\delta^{18}\text{O}$  analyses, and Dylan Dorey, Katherine Halter, Heidi Lauchstedt, and Jake Tholen (the Kartchner Caverns Cave Unit & Natural Resources Team) for collecting meteoric waters. TEH thanks Kelsey Dyez and Giuseppe Lucia for advice on milling stalagmite samples and thanks Hagit Affek for helpful comments on Fig. 5. We thank the following people and organizations for facilitating cave access and permits for cave work: J. Trout, US Forest Service (JEC at Cave of the Bells), the Ely District of the Bureau of Land Management (MSL at Leviathan Cave), and Ben Roberts, Gretchen Baker, and the staff of Great Basin National Park (MSL, DM and RFD, Lehman Caves). This work was supported by funding to BHP and NEL from the University of Michigan. JEC acknowledges support from NSF 1702271 and 0903093, and assistance from K. Dyez.

## APPENDIX A. SUPPLEMENTARY MATERIAL

Supplementary data to this article can be found online at <https://doi.org/10.1016/j.gca.2021.11.002>.

## REFERENCES

- Adams D. K. and Comrie A. C. (1997) The North American Monsoon. *Bull. Am. Meteorol. Soc.* **78**(10), 2197–2213.
- Affek H. P., Bar-Matthews M., Ayalon A., Matthews A. and Eiler J. M. (2008) Glacial/interglacial temperature variations in Soreq cave speleothems as recorded by 'clumped isotope' thermometry. *Geochim. Cosmochim. Acta* **72**, 5351–5360.
- Affek H. P., Matthews A., Ayalon A., Bar-Matthews M., Burstyn Y., Zaarur S. and Zilberman T. (2014) Accounting for kinetic isotope effects in Soreq Cave (Israel) speleothems. *Geochim. Cosmochim. Acta* **143**, 303–318.
- Affek H. P. and Zaarur S. (2014) Kinetic isotope effect in CO<sub>2</sub> degassing: Insight from clumped and oxygen isotopes in laboratory precipitation experiments. *Geochim. Cosmochim. Acta* **143**, 319–330.
- Affolter S., Häuselmann A., Fleitmann D., Edwards R. L., Cheng H. and Leuenberger M. (2019) Central Europe temperature constrained by speleothem fluid inclusion water isotopes over the past 14,000 years. *Sci. Adv.* **5**, 1–9.
- Affolter S., Häuselmann A. D., Fleitmann D., Häselmann P. and Leuenberger M. (2015) Triple isotope ( $\delta\text{D}$ ,  $\delta^{17}\text{O}$ ,  $\delta^1\text{O}$ ) study on precipitation, drip water and speleothem fluid inclusions for a Western Central European cave (NW Switzerland). *Quat. Sci. Rev.* **127**, 73–89.
- Ampuero A., Stríkis N. M., Apaéstegui J., Vuille M., Novello V. F., Espinoza J. C., Cruz F. W., Vonhof H., Mayta V. C., Martins V. T. S., Cordeiro R. C., Azevedo V. and Sifeddine A. (2020) The forest effects on the isotopic composition of rainfall in the northwestern Amazon Basin. *J. Geophys. Res. Atmos.* **125**, 1–16.
- Aron P. G., Levin N. E., Beverly E. J., Huth T. E., Passey B. H., Pelletier E. M., Poulsen C. J., Winkelstern I. Z. and Yarian D. A. (2021) Triple oxygen isotopes in the water cycle. *Chem. Geol.* **565** 120026.
- Asmerom Y., Polyak V., Burns S. and Rasmussen J. (2007) Solar forcing of Holocene climate: New insights from a speleothem record, southwestern United States. *Geology* **35**, 1–4.
- Asmerom Y., Polyak V. J. and Burns S. J. (2010) Variable winter moisture in the southwestern United States linked to rapid glacial climate shifts. *Nat. Geosci.* **3**, 114–117.
- Asmerom Y., Polyak V. J., Rasmussen J. B., Burns S. J. and Lachnit M. (2013) Multidecadal to multicentury scale collapses of Northern Hemisphere monsoons over the past millennium. *Proc. Natl. Acad. Sci. USA* **110**(24), 9651–9656.
- Baldini J. U., McDermott F., Hoffmann D. L., Richards D. A. and Clipson N. (2008) Very high-frequency and seasonal cave atmosphere  $\text{Pco}_2$  variability: implications for stalagmite growth and oxygen isotope-based paleoclimate records. *Ear. Plan. Sci. Lett.* **272**, 118–129.
- Banner J. L., Guilfoyle A., James E. W., Stern L. A. and Musgrove M. (2007) Seasonal variations in modern speleothem calcite growth in central Texas, U.S.A. *J. Sediment. Res.* **77**, 615–622.
- Barkan E., Affek H. P., Luz B., Bergel S., Voarintsoa N. R. G. and Musan I. (2019) Calibration of  $\delta^{17}\text{O}$  and  $^{17}\text{O}_{\text{excess}}$  of three international standards - IAEA603, NBS19 and NBS18. *Rapid Commun. Mass Spectrom.* **33**, 737–740.
- Barkan E. and Luz B. (2005) High precision measurements of  $^{17}\text{O}/^{16}\text{O}$  and  $^{18}\text{O}/^{16}\text{O}$  of  $\text{O}_2$  in  $\text{H}_2\text{O}$ . *Rapid Commun. Mass Spectrom.* **19**, 3737–3742.
- Barkan E. and Luz B. (2007) Diffusivity fractionations of  $\text{H}_2^{16}\text{OH}/\text{H}_2^{17}\text{OH}$  and  $\text{H}_2^{16}\text{OH}/\text{H}_2^{18}\text{O}$  in air and their implications for isotope hydrology. *Rapid Commun. Mass Spectrom.* **21**, 2999–3005.
- Barth C., Boyle D. P., Hatchett B. J., Bassett S. D., Garner C. B. and Adams K. D. (2016) Late Pleistocene climate inferences from a water balance model of Jakes Valley, Nevada (USA). *J. Paleolimnol.* **56**, 109–122.
- Beck W. C., Grossman E. L. and Morse J. W. (2005) Experimental studies of oxygen isotope fractionation in the carbonic acid system at 15°, 25°, and 40°C. *Geochim. Cosmochim. Acta* **69** (14), 3493–3503.
- Bergel S. J., Barkan E., Stein M. and Affek H. P. (2020) Carbonate  $^{17}\text{O}_{\text{excess}}$  as a paleo-hydrology proxy: Triple oxygen isotope fractionation between  $\text{H}_2\text{O}$  and biogenic aragonite, derived from freshwater mollusks. *Geochim. Cosmochim. Acta* **275**, 36–47.
- Berger A. and Loutre M. F. (1991) Insolation values for the climate of the last 10 million years. *Quat. Sci. Rev.* **10**(4), 297–317.
- Bershaw J., Hansen D. D. and Schauer A. J. (2020) Deuterium excess and  $^{17}\text{O}_{\text{excess}}$  variability in meteoric water across the Pacific Northwest, USA. *Tellus B: Chem. Phys. Meteorol.* **72**(1), 1–14.
- Bowen G. J. and Revenaugh J. (2003) Interpolating the isotopic composition of modern meteoric precipitation. *Water Resour. Res.* **39**(10), 299.

- Braconnot P., Harrison S. P., Kageyama M., Bartlein P. J., Masson-Delmotte V., Abe-Ouchi A., Otto-Bliesner B. and Zhao Y. (2012) Evaluation of climate models using palaeoclimatic data. *Nat. Clim. Change* **2**, 417–424.
- Braconnot, P., Harrison, S. P., Otto-Bliesner, B., Abe-Ouchi, A., Jungclaus, J., Peterschmitt, J.-Y., 2011. The Paleoclimate Modeling Intercomparison Project contribution to CMIP5. CLIVAR Exchanges No. 56, 16(2), 15–19.
- Brand W. A., Assonov S. S. and Coplen T. B. (2010) Correction for the  $^{17}\text{O}$  interference in  $\delta(^{13}\text{C})$  measurements when analyzing CO with stable isotope mass spectrometry (IUPAC Technical Report). *Pure Appl. Chem.* **82**(8), 1719–1733.
- Cao X. B. and Liu Y. (2011) Equilibrium mass-dependent fractionation relationships for triple oxygen isotopes. *Geochim. Cosmochim. Acta* **75**, 7435–7445.
- Cheng H., Edwards R. L., Broecker W. S., Denton G. H., Kong X., Wang Y., Zhang R. and Wang X. (2009) Ice age terminations. *Science* **326**, 248–252.
- Cheng H., Sinha A., Wang X., Cruz F. W. and Edwards R. L. (2012) The Global Paleomonsoon as seen through speleothem records from Asia and the Americas. *Clim. Dyn.* **39**, 1045–1062.
- Cheng H., Sinha A., Verheyden S., Nader F. H., Li X. L., Zhang P. Z., Yin J. J., Yi L., Peng Y. B., Rao Z. G., Ning Y. F. and Edwards R. L. (2015) The climate variability in northern Levant over the past 20,000 years. *Geophys. Res. Lett.* **42**, 8641–8650.
- Cheng H., Spötl C., Breitenbach S. F. M., Sinha A., Wassenburg J. A., Jochum K. P., Scholz D., Li X., Yi L., Peng Y., Lv Y., Zhang P., Votintseva A., Longinov V., Ning Y., Kathayat G. and Edwards R. L. (2016) Climate variations of Central Asia on orbital to millennial timescales. *Sci. Rep.* **6**, 1–11.
- Coplen T. B. (2007) Calibration of the calcite–water oxygen-isotope geothermometer at Devils Hole, Nevada, a natural laboratory. *Geochim. Cosmochim. Acta* **71**(16), 3948–3957.
- Craig H. (1957) Isotopic standards for carbon and oxygen and correction factors for mass-spectrometric analysis of carbon dioxide. *Geochim. Cosmochim. Acta* **12**, 133–149.
- Criss R. E. (1999) Principles of Stable Isotope Distribution. Oxford University Press, New York.
- Daëron M., Guo W., Eiler J., Genty D., Blamart D., Boch R., Drysdale R., Maire R., Wainer K. and Zanchetta G. (2011)  $^{13}\text{C}^{\text{O}}$  clumping in speleothems: Observations from natural caves and precipitation experiments. *Geochim. Cosmochim. Acta* **75**, 3303–3317.
- Dansgaard W. (1964) Stable isotopes in precipitation. *Tellus* **16**(4), 436–468.
- Day C. C. and Henderson G. M. (2011) Oxygen isotopes in calcite grown under cave-analogue conditions. *Geochim. Cosmochim. Acta* **75**, 3956–3972.
- Deininger M., Fohlmeister J., Scholz D. and Mangini A. (2012) Isotope disequilibrium effects: The influence of evaporation and ventilation effects on the carbon and oxygen isotope composition of speleothem – A model approach. *Geochim. Cosmochim. Acta* **96**, 57–79.
- Deininger M. and Scholz D. (2019) ISOLUTION 1.0: an ISOtope evoLUTION model describing the stable oxygen ( $\delta^1\text{O}$ ) and carbon ( $\delta^{13}\text{C}$ ) isotope values of speleothems. *Int. J. Speadol.* **48** (1), 21–32.
- Denniston R. F., Asmerom Y., Polyak V., Dorale J. A., Carpenter S. J., Trodick C., Hoye B. and González L. A. (2007) Synchronous millennial-scale climatic changes in the Great Basin and the North Atlantic during the last interglacial. *Geology* **35**(7), 619–622.
- Dorale J. A. and Liu Z. (2009) Limitations of Hendy test criteria in judging the paleoclimatic suitability of speleothems and the need for replication. *J. Cave Karst. Stud.* **71**, 73–80.
- Dreybrodt W. and Scholz D. (2011) Climatic dependence of stable carbon and oxygen isotope signals recorded in speleothems: From soil water to speleothem calcite. *Geochim. Cosmochim. Acta* **75**, 734–752.
- Dütsch M., Pfahl S. and Sodemann H. (2017) The impact of nonequilibrium and equilibrium fractionation on two different deuterium excess definitions. *J. Geophys. Res. Atmos.* **122**, 12732–12746.
- Eastoe C. J. and Dettman D. L. (2016) Isotope amount effects in hydrologic and climate reconstructions of monsoon climates: Implications of some long-term data sets for precipitation. *Chem. Geol.* **430**, 78–89.
- EL-Shenawy M. I., Kim S.-T. and Schwarcz H. P. (2020) Carbon and oxygen isotope systematics in cave environments: Lessons from an artificial cave “McMaster Cave”. *Geochim. Cosmochim. Acta* **272**, 137–159.
- Fairchild I. J., Borsato A., Tooth A. F., Frisia S., Hawkesworth C. J., Huang Y., McDermott F. and Spiro B. (2000) Controls on trace element (Sr–Mg) compositions of carbonate cave waters: implications for speleothem climatic records. *Chem. Geol.* **166**, 255–269.
- Fairchild I. J. and Treble P. C. (2009) Trace elements in speleothems as recorders of environmental change. *Quat. Sci. Rev.* **28**, 449–468.
- Fröhlich, K., Gibson, J.J., Aggarwal, P.K., 2002. Deuterium excess in precipitation and its climatological significance. International Atomic Energy Agency report IAEA-CSP-13/P, 34(10), 54–66.
- Friedman I. and O’Neil J. R. (1977) Compilation of Stable Isotope Fractionation Factors of Geochemical Interest. In *Data of Geochemistry*, Fleischer M., ed.. U.S. Geol. Survey Professional Paper, 440-KK.
- Frumkin A. and Stein M. (2004) The Sahara-East Mediterranean dust and climate connection revealed by strontium and uranium isotopes in a Jerusalem speleothem. *Ear. Plan. Sci. Lett.* **217**, 451–464.
- Gásquez F., Calaforra J. M., Evans N. P. and Hodell D. A. (2017) Using stable isotopes ( $\delta^{17}\text{O}$ ,  $\delta^1\text{O}$  and  $\delta\text{D}$ ) of gypsum hydration water to ascertain the role of water condensation in the formation of subaerial gypsum speleothems. *Chem. Geol.* **452**, 34–46.
- Gázquez F., Bauska T. K., Comas-Bru L., Ghaleb B., Calaforra J.-M. and Hodell D. A. (2020) The potential of gypsum speleothems for paleoclimatology: application to the Iberian Roman Human Period. *Sci. Rep.* **10**, 4705.
- Gázquez F., Morellón M., Bauska T., Herwartz D., Surma J., Moreno A., Staubwasser M., Valero-Garcés B., Delgado-Huertas A. and Hodell D. A. (2018) Triple oxygen and hydrogen isotopes of gypsum hydration water for quantitative paleo-humidity reconstruction. *Ear. Plan. Sci. Lett.* **481**, 177–188.
- Ghosh P., Adkins J., Affek H., Balta B., Guo W., Schauble E. A., Schrag D. and Eiler J. M. (2006)  $^{13}\text{C}–^{18}\text{O}$  bonds in carbonate minerals: A new kind of paleothermometer. *Geochim. Cosmochim. Acta* **70**, 1439–1456.
- Guo W. and Zhou C. (2019a) Patterns and controls of disequilibrium isotope effects in speleothems: Insights from an isotope-enabled diffusion–reaction model and implications for quantitative thermometry. *Geochim. Cosmochim. Acta* **267**, 196–226.
- Guo W. and Zhou C. (2019b) Triple oxygen isotope fractionation in the DIC–HO–CO system: A numerical framework and its implications. *Geochim. Cosmochim. Acta* **246**, 541–564.
- Hansen M., Scholz D., Schöne B. R. and Spötl C. (2019) Simulating speleothem growth in the laboratory: Determination of the stable isotope fractionation ( $\delta^{13}\text{C}$  and  $\delta^1\text{O}$ ) Between HO, DIC, and CaCO. *Chem. Geol.* **509**, 20–44.

- Harbert R. S. and Nixon K. C. (2018) Quantitative Late Quaternary climate reconstruction from plant macrofossil communities in western North America. *Open Quat.* **4**(8), 1–13.
- Hayles J., Gao C., Cao X., Liu Y. and Bao H. (2018) Theoretical calibration of the triple oxygen isotope thermometer. *Geochim. Cosmochim. Acta* **235**, 237–245.
- He S., Jackisch D., Samanta D., Yu Yi P. K., Liu G., Wang X. and Goodkin N. F. (2021) Understanding tropical convection through triple oxygen isotopes of precipitation from the maritime continent. *J. Geophys. Res. Atmos.* **126**, 1–14.
- Hendy C. H. (1971) The isotopic geochemistry of speleothems—I: The calculations of the effects of different modes of formation on the isotopic composition of speleothems and their applicability as paleoclimate indicators. *Geochim. Cosmochim. Acta* **35**, 801–824.
- Henkes G. A., Passey B. H., Grossman E. L., Shenton B. J., Pérez-Huerta A. and Yancey T. E. (2014) Temperature limits for preservation of primary calcite clumped isotope paleotemperatures. *Geochim. Cosmochim. Acta* **139**, 362–382.
- Higgins R. W., Yao Y. and Wang X. L. (1997) Influence of the North American Monsoon system on the U.S. summer precipitation regime. *J. Climate* **10**, 2600–2622.
- Horita J. and Wesolowski D. J. (1994) Liquid-vapor fractionation of oxygen and hydrogen isotopes of water from the freezing to the critical temperature. *Geochim. Cosmochim. Acta* **58**(16), 3425–3437.
- Hudson A. M., Hatchett B. J., Quade J., Boyle D. P., Bassett S. D., Ali G. and Santos M. G. De lo (2019) North-south dipole in winter hydroclimate in the western United States during the last deglaciation. *Sci. Rep.* **9**(4826), 1–12.
- Huth T. E., Cerling T. E., Marchetti D. W., Bowling D. R., Ellwein A. L., Passey B. H., Fernandez D. P., Valley J. W. and Orland I. J. (2020) Laminated soil carbonate rinds as a paleoclimate archive of the Colorado Plateau. *Geochim. Cosmochim. Acta* **282**, 227–244.
- IAEA, 2021. Reference Materials. [Online] Available at: <https://nucleus.iaea.org/sites/referencematerials/SitePages/Home.aspx> [Accessed 12 Jan 2021].
- Ibarra D. E., Kukla T., Methner K. A., Mulch A. and Chamberlain C. P. (2021) Reconstructing past elevations from triple oxygen isotopes of lacustrine chert: application to the Eocene Nevadaplano, Elko Basin, Nevada, United States. *Front. Earth Sci.* **9** 62886.
- Kim S.-T., Coplen T. B. and Horita J. (2015) Normalization of stable isotope data for carbonatite minerals: Implementation of IUPAC guidelines. *Geochim. Cosmochim. Acta* **158**, 276–289.
- Kim S.-T., Mucci A. and Taylor B. E. (2007) Phosphoric acid fractionation factors for calcite and aragonite between 25 and 75 °C: revisited. *Chem. Geol.* **246**, 135–146.
- Kim S.-T. and O'Neil J. R. (1997) Equilibrium and non-equilibrium oxygen isotope effects in synthetic carbonates. *Geochim. Cosmochim. Acta* **61**(16), 3461–3475.
- Kukla T., Winnick M. J., Maher K., Ibarra D. E. and Chamberlain C. P. (2019) The sensitivity of terrestrial  $\delta^{18}\text{O}$  gradients to hydroclimate evolution. *J. Geophys. Res. Atmos.* **124**, 563–582.
- Kulge T. and Affek H. P. (2012) Quantifying kinetic fractionation in Bunker Cave speleothems using  $\Delta_{47}$ . *Quat. Sci. Rev.* **49**, 82–94.
- Lachniet M., Asmerom Y., Polyak V. and Denniston R. (2017) Arctic cryosphere and Milankovitch forcing of Great Basin paleoclimate. *Sci. Rep.* **7**, 1–10.
- Lachniet M. S. (2009) Climatic and environmental controls on speleothem oxygen-isotope values. *Quat. Sci. Rev.* **28**, 413–432.
- Lachniet M. S., Asmerom Y., Polyak V. and Denniston R. (2020) Great Basin paleoclimate and aridity linked to Arctic warming and tropical Pacific Sea surface temperatures. *Paleoceanogr. Paleoclimatol.* **35**, 1–22.
- Lachniet M. S., Denniston R. F., Asmerom Y. and Polyak V. J. (2014) Orbital control of western North America atmospheric circulation and climate over two glacial cycles. *Nat. Comm.* **5**, 1–8.
- Landais A., Barkan E. and Luz B. (2008) Record of  $\delta^1\text{O}$  and  $^{17}\text{O}$ -excess in ice from Vostok Antarctica during the last 150,000 years. *Geophys. Res. Lett.* **35**, L02709.
- Landais A., Risi C., Bony S., Vimeux F., Descroix L., Falourd S. and Bouygues A. (2010) Combined measurements of  $^{17}\text{O}_{\text{excess}}$  and d-excess in African monsoon precipitation: Implications for evaluating convective parameterizations. *Ear. Plan. Sci. Lett.* **298**, 104–112.
- Li S., Levin N. E. and Chesson L. A. (2015) Continental scale variation in  $^{17}\text{O}$ -excess of meteoric waters in the United States. *Geochim. Cosmochim. Acta* **164**, 110–126.
- Liang Y., Zhao K., Edwards R. L., Wang Y., Shao Q., Zhang Z., Zhao B., Wang Q., Cheng H. and Kong X. (2020) East Asian monsoon changes early in the last deglaciation and insights into the interpretation of oxygen isotope changes in the Chinese stalagmite record. *Quat. Sci. Rev.* **250**, 1–11.
- Lisiecki L. E. and Raymo M. E. (2005) A Pliocene-Pleistocene stack of 57 globally distributed benthic  $\delta^{18}\text{O}$  records. *Paleoceanography* **20**, 1–17.
- Liu Z., Bowen G. J. and Welker J. M. (2010) Atmospheric circulation is reflected in precipitation isotope gradients over the conterminous United States. *J. Geophys. Res.* **115**, 1–14.
- Lundeen Z., Brunelle A., Burns S. J., Polyak V. and Asmerom Y. (2013) A speleothem record of Holocene paleoclimate from the northern Wasatch Mountains, southeast Idaho, USA. *Quat. Int.* **310**, 83–95.
- Luz B. and Barkan E. (2010) Variations of  $^{17}\text{O}/\text{O}$  and  $^{18}\text{O}/\text{O}$  in meteoric waters. *Geochim. Cosmochim. Acta* **74**, 6276–6286.
- Madsen D. B., Rhode D., Grayson D. K., Broughton J. M., Livingston S. D., Hunt J., Quade J., Schmitt D. N. and Shaver I. I. I. M. W. (2001) Late Quaternary environmental change in the Bonneville basin, western USA. *Palaeogeogr. Palaeoclimatol. Palaeoecol.* **167**, 243–271.
- Maher B. A. and Thompson R. (2012) Oxygen isotopes from Chinese caves: records not of monsoon rainfall but of circulation regime. *J. Quat. Sci.* **27**(6), 615–624.
- Marchetti D. W., Harris M. S., Bailey C. M., Cerling T. E. and Berman S. (2011) Timing of glaciation and last glacial maximum paleoclimate estimates from the Fish Lake Plateau, Utah. *Quat. Res.* **75**, 183–195.
- Mattey D. P., Atkinson T. C., Barker J. A., Fisher R., Latin J.-P., Durrell R. and Ainsworth M. (2016) Carbon dioxide, ground air and carbon cycling in Gibraltar karst. *Geochim. Cosmochim. Acta* **184**, 88–113.
- McCrea J. M. (1950) On the isotopic chemistry of carbonates and a paleotemperature scale. *J. Chem. Phys.* **18**, 849–857.
- McGarry S., Bar-Matthews M., Matthews A., Vaks A., Schilman B. and Ayalon A. (2004) Constraints on hydrological and paleotemperature variations in the Eastern Mediterranean region in the last 140 ka given by the  $\delta\text{D}$  values of speleothemfluid inclusions. *Quat. Sci. Rev.* **23**, 919–934.
- Meckler A. N., Vonhof H. and García Martíne (2021) Temperature reconstructions using speleothems. *Elements* **17**, 101–106.
- Mickler P. J., Banner J. L., Stern L., Asmerom Y., Edwards R. L. and Ito E. (2004) Stable isotope variations in modern tropical speleothems: Evaluating equilibrium vs. kinetic isotope effects. *Geochim. Cosmochim. Acta* **68**(21), 4381–4393.
- Mickler P. J., Stern L. A. and Banner J. L. (2006) Large kinetic isotope effects in modern speleothems. *Geol. Soc. Am. Bull.* **118**(1/2), 65–81.

- Mickler P. J., Carlson P., Banner J. L., Breecker D. O., Stern L. and Guilfoyle A. (2019) Quantifying carbon isotope disequilibrium during in-cave evolution of drip water along discreet flow paths. *Geochim. Cosmochim. Acta* **244**, 182–196.
- Miller M. F. (2002) Isotopic fractionation and the quantification of  $^{17}\text{O}$  anomalies in the oxygen three-isotope system: an appraisal and geochemical significance. *Geochim. Cosmochim. Acta* **66** (11), 1881–1889.
- Mook, W.G., 2000. Environmental isotopes in the hydrological cycle: Volume 1: Introduction (Theory, Methods, Review). International Hydrological Programme, Technical Documents in Hydrology No. 39, vol. 1, Paris, France: UNESCO.
- Musgrove M. and Banner J. L. (2004) Controls on the spatial and temporal variability of vadose dripwater geochemistry: Edwards Aquifer, central Texas. *Geochim. Cosmochim. Acta* **68**, 1007–1020.
- Orland I. J., He F., Bar-Matthews M., Chen G., Ayalon A. and Kutzbach J. E. (2019) Resolving seasonal rainfall changes in the Middle East during the last interglacial period. *Proc. Natl. Acad. Sci. USA* **116**(59), 24985–24990.
- Oster J. L., Montañez I. P., Guilderson T. P., Sharp W. D. and Banner J. L. (2010) Modeling speleothem  $\delta^{13}\text{C}$  variability in a central Sierra Nevada cave using  $^{14}\text{C}$  and  $^{87}\text{Sr}/^{86}\text{Sr}$ . *Geochim. Cosmochim. Acta* **74**, 5228–5242.
- Oster J. L., Ibarra D. E., Winnick M. J. and Maher K. (2015) Steering of westerly storms over western North America at the Last Glacial Maximum. *Nat. Geosci.* **8**, 201–205.
- Passey B. H., Hu H., Ji H., Montanari S., Li S., Henkes G. A. and Levin N. E. (2014) Triple oxygen isotopes in biogenic and sedimentary carbonates. *Geochim. Cosmochim. Acta* **141**, 1–25.
- Passey B. H. and Ji H. (2019) Triple oxygen isotope signatures of evaporation in lake waters and carbonates: A case study from the western United States. *Eur. Plan. Sci. Lett.* **518**, 1–12.
- Passey B. H. and Levin N. E. (2021) Triple oxygen isotopes in meteoric waters, carbonates, and biologicalapatites: Implications for continental paleoclimate reconstruction. *Rev. Mineral. Geochem.* **86**, 429–462.
- Passey B. H., Levin N. E., Cerling T. E., Brown F. H. and Eiler J. M. (2010) High temperature environments of human evolution from bond ordering in paleosol carbonates. *Proc. Natl. Acad. Sci. USA* **107**, 11245–11249.
- Pausata F. S., Battisti D. S., Nisancioglu K. H. and Bitz C. M. (2011) Chinese stalagmite  $\delta^{18}\text{O}$  controlled by changes in the Indian monsoon during a simulated Heinrich event. *Nat. Geosci.* **4**, 474–480.
- Pfahl S. and Sodemann H. (2014) What controls deuterium excess in global precipitation. *Clim. Past* **10**, 771–781.
- Polyak V. J., Asmerom Y. and Lachniet M. S. (2017) Rapid speleothem  $\delta^{13}\text{C}$  change in southwestern North America coincident with Greenland stadial 20 and the Toba (Indonesia) supereruption. *Geology* **45**(9), 843–846.
- Quirk B. J., Moore J. R., Laabs B. J. C., Plummer M. A. and Caffee M. W. (2020) Latest Pleistocene glacial and climate history of the Wasatch Range, Utah. *Quat. Sci. Rev.* **238**, 1–17.
- Rasmussen S. O., Bigler M., Blockley S. P., Blunier T., Buchardt S. L., Clausen H. B., Cvijanovic I., Dahl-Jensen D., Johnsen S. J., Fischer H., Gkinis V., Guillec M., Hoek W. Z., Lowe J. J., Pedro J. B., Popp T., Seierstad I. K., Steffensen J. P., Svensson A. M., Vallelonga P., Vinther B. M., Walker M. J. C., Wheatley J. J. and Winstrup M. (2014) A stratigraphic framework for abrupt climatic changes during the Last Glacial period based on three synchronized Greenland ice-core records: refining and extending the INTIMATE event stratigraphy. *Quat. Sci. Rev.* **106**, 14–28.
- Reinemann S. A., Porinchu D. F., Bloom A. M., Mark B. G. and Box J. E. (2009) A multi-proxy paleolimnological reconstruc-
- tion of Holocene climate conditions in the Great Basin, United States. *Quat. Res.* **72**, 347–358.
- Richards D. A. and Dorale J. A. (2003) Uranium-series chronology and environmental applications of speleothems. *Rev. Mineral. Geochem.* **52**(1), 407–460.
- Risi C., Landais A., Bony S., Jean J., Masson-Delmotte V. and Vimeux F. (2010) Understanding the  $\text{O}-17$  excess glacial-interglacial variations in Vostok precipitation. *J. Geophys. Res. Atmos.* **115**, 1–15.
- Risi C., Landais A., Winkler R. and Vimeux F. (2013) Can we determine what controls the spatio-temporal distribution of d-excess and  $\text{O}-17$ -excess in precipitation using the LMDZ general circulation model? *Clim. Past* **9**(5), 2173–2193.
- Ryan W. F., Carbotte S. M., Coplan J., O'Hara S., Melkonian A., Arko R., Weissel R. A., Ferrini V., Goodwillie A., Nitsche F., Bonczkowski J. and Zemsky R. (2009) Global multi-resolution topography (GMRT) synthesis data set. *Geochem. Geophys. Geosyst.* **10**, Q03014.
- Santrock J., Studley S. A. and Hayes J. M. (1985) Isotopic analyses based on the mass spectrum of carbon dioxide. *Anal. Chem.* **57**, 1444–1448.
- Schaube E. A. and Young E. D. (2021) Mass dependence of equilibrium oxygen isotope fractionation in carbonate, nitrate, oxide, perchlorate, phosphate, silicate, and sulfate minerals. *Rev. Mineral. Geochem.* **86**, 137–178.
- Schauer A. J., Kelson J., Saenger C. and Huntington K. W. (2016) Choice of  $^{17}\text{O}$  correction affects clumped isotope ( $\Delta$ ) values of CO measured with mass spectrometry. *Rapid Commun. Mass Spectrom.* **30**, 2607–2616.
- Schoenemann S. W., Schaer A. J. and Steig E. J. (2013) Measurement of SLAP2 and GISP  $\delta^{17}\text{O}$  and proposed VSMOW-SLAP normalization for  $\delta^{17}\text{O}$  and  $^{17}\text{O}$ excess. *Rapid Commun. Mass Spectrom.* **27**, 582–590.
- Schoenemann S. W. and Steig E. J. (2016) Seasonal and spatial variations of  $^{17}\text{O}$ excess and dexcess in Antarctic precipitation: Insights from an intermediate complexity isotope model. *J. Geophys. Res. Atmos.* **121**, 11215–11247.
- Scholz D., Mülinghaus C. and Mangini A. (2009) Modelling  $\delta^{13}\text{C}$  and  $\delta^1\text{O}$  in the solution layer on stalagmite surfaces. *Geochim. Cosmochim. Acta* **73**, 2592–2602.
- Schuman B. N. and Serravezza M. (2017) Patterns of hydroclimatic change in the Rocky Mountains and surrounding regions since the last glacial maximum. *Quat. Sci. Rev.* **173**, 58–77.
- Sha L., Mahata S., Duan P., Luz B., Zhang P., Baker J., Zong B., Ning Y., Brahim Y. A., Zhang H., Edwards R. L. and Cheng H. (2020) A novel application of triple oxygen isotope ratios of speleothems. *Geochim. Cosmochim. Acta* **270**, 360–378.
- Sharp Z. D., Wostbrock J. A. G. and Pack A. (2018) Mass-dependent triple oxygen isotope variations in terrestrial materials. *Geochem. Persp. Let.* **7**, 27–31.
- Sharp Z. D. and Wostbrock J. A. G. (2021) Standardization for the triple oxygen isotope system: waters, silicates, carbonates, air, and sulfates. *Rev. Mineral. Geochem.* **86**, 179–196.
- Spötl C., Fairchild I. J. and Tooth A. F. (2005) Cave air control on dripwater geochemistry, Obir Caves (Austria): Implications for speleothem deposition in dynamically ventilated caves. *Geochim. Cosmochim. Acta* **69**(10), 2451–2468.
- Steponaitis E., Andrews A., McGee D., Quade J., Hsieh Y.-T., Broecker W. S., Shuman B. N., Burns S. J. and Cheng H. (2015) Mid-Holocene drying of the U.S. Great Basin recorded in Nevada speleothems. *Quat. Sci. Rev.* **127**, 174–185.
- Stute M., Clark J. F., Schlosser P. and Broecker W. S. (1995) A 30,000 yr continental paleotemperature record derived from noble gases dissolved in groundwater from the San Juan Basin, New Mexico. *Quat. Res.* **43**, 209–220.

- Surma J., Assonov S., Bolourchi M. J. and Staubwasser M. (2015) Triple oxygen isotope signatures in evaporated water bodies from the Sistan Oasis. *Iran. Geophys. Res. Lett.* **42**, 8456–8462.
- Surma J., Assonov S., Herwartz D., Voigt C. and Staubwasser M. (2018) The evolution of  $^{17}\text{O}$ -excess in surface water of the arid environment during recharge and evaporation. *Sci. Rep.* **8** (4972), 1–10.
- Svensson A., Andersen K. K., Bigler M., Clausen H. B., Dahl-Jensen D., Davies S. M., Johnsen S. J., Muscheler R., Parrenin F., Rasmussen S. O., Röhlisberger R., Seierstad I., Steffensen J. P. and Vinther B. M. (2008) A 60 000 year Greenland stratigraphic ice core chronology. *Clim. Past.* **4**, 47–57.
- Tierney J. E., Zhu J., King J., Malevich S. B., Hakim G. J. and Poulsen C. J. (2020) Glacial cooling and climate sensitivity revisited. *Nature* **584**, 569–573.
- Truebe, S.A., 2016. Past climate, modern caves, and future resource management in speleothem paleoclimatology. (PhD thesis, pp. 1–265).
- Uechi Y. and Uemura R. (2019) Dominant influence of the humidity in the moisture source region on the  $^{17}\text{O}$ -excess in precipitation on a subtropical island. *Ear. Plan. Sci. Lett.* **513**, 20–28.
- Uemura R., Barkan E., Abe O. and Luz B. (2010) Triple isotope composition of oxygen in atmospheric water vapor. *Geophys. Res. Lett.* **37**, 1–4.
- Uemura R., Yonezawa N., Yoshimura K., Asami R., Kadena H., Yamada K. and Yoshida N. (2012) Factors controlling isotopic composition of precipitation on Okinawa Island, Japan: Implications for paleoclimate reconstruction in the East Asian Monsoon region. *J. Hydrol.* **475**, 314–322.
- Voorhies N. R. G., Barkan E., Bergel S., Vieten R. and Affek H. P. (2020) Triple oxygen isotope fractionation between  $\text{CaCO}_3$  and  $\text{H}_2\text{O}$  in inorganically precipitated calcite and aragonite. *Chem. Geol.* **539**, 1–8.
- Voigt C., Herwartz D., Dorador C. and Staubwasser M. (2021) Triple oxygen isotope systematics of evaporation and mixing processes in a dynamic desert lake system. *Hydrol. Earth Syst. Sci.* **25**, 1211–1228.
- Wagner J. D. M., Cole J. E., Beck J. W., Patchett P. J., Henderson G. M. and Barnett H. R. (2010) Moisture variability in the southwestern United States linked to abrupt glacial climate change. *Nat. Geosci.* **3**, 110–113.
- Wainer K., Genty D., Blamart D., Daëron M., Bar-Matthews M., Vonhof H., Dublyansky Y., Pons-Branchu E., Thomas L., Calsteren P. va, Quinif Y. and Caillon N. (2011) Speleothem record of the last 180 ka in Villars cave (SW France): Investigation of a large  $\delta^{18}\text{O}$  shift between MIS6 and MIS5. *Quat. Sci. Rev.* **30**, 130–146.
- Wang X., Edwards R. L., Auler A. S., Cheng H., Kong X., Wang Y., Cruz F. W., Dorale J. A. and Chiang H.-W. (2017) Hydroclimate changes across the Amazon lowlands over the past 45,000 years. *Nature* **541**, 204–207.
- Wang Y. J., Cheng H., Edwards R. L., An Z. S., Wu J. Y., Shen C.-C. and Dorale J. A. (2001) A high-resolution absolute-dated Late Pleistocene monsoon record from Hulu Cave, China. *Science* **294**, 2345–2348.
- Welker J. M. (2012) El Niño effects on d18O, d2H and d-excess values in precipitation across the U.S. using a high-density, long-term network (USNIP). *Rapid. Commun. Mass Spectrom.* **26**, 1893–1898.
- Winograd I. J., Riggs A. C. and Coplen T. B. (1998) The relative contributions of summer and cool-season precipitation to groundwater recharge, Spring Mountains, Nevada, USA. *Hydrogeol. J.* **6**(1), 77–93.
- Wong C. I. and Banner J. L. (2010) Response of cave air  $\text{CO}_2$  and drip water to brush clearing in central Texas: implications for recharge and soil  $\text{CO}_2$  dynamics. *Biogeosciences* **115**, G04018.
- Wong C. I. and Breecker D. O. (2015) Advancements in the use of speleothems as climate archives. *Quat. Sci. Rev.* **127**, 1–18.
- Wostbrock J. A., Brand U., Coplen T. B., Swart P. K., Carlson S. J., Brearley A. J. and Sharp Z. D. (2020a) Calibration of carbonate–water triple oxygen isotope fractionation: Seeing through diagenesis in ancient carbonates. *Geochim. Cosmochim. Acta* **288**, 369–388.
- Wostbrock J. A., Cano E. J. and Sharp Z. D. (2020b) An internally consistent triple oxygen isotope calibration of standards for silicates, carbonates, and air relative to VSMOW2 and SLAP2. *Chem. Geol.* **533**, 1–9.
- Yin J.-J., Yuan D.-X., Li H.-C., Cheng H., Li T.-Y., Edwards R. L., Lin Y.-S., Qin J.-M., Tang W., Zhao Z.-Y. and Mii H.-S. (2014) Variation in the Asian monsoon intensity and dry–wet conditions since the Little Ice Age in central China revealed by an aragonite stalagmite. *Clim. Past* **10**, 1803–1816.
- Yuan D., Cheng H., Edwards R. L., Dykoski C. A., Kelly M. J., Zhang M., Qing J., Lin Y., Wang Y., Wu J., Dorale J. A., An Z. and Cai Y. (2004) Timing, duration, and transitions of the last interglacial Asian monsoon. *Science* **304**, 575–578.
- Zaarur S., Affek H. P. and Brandon M. T. (2013) A revised calibration of the clumped isotope thermometer. *Earth Planet. Sci. Lett.* **382**, 47–57.
- Zhou J., Lundstrom C. C., Fouke B., Panno S., Hackley K. and Curry B. (2005) Geochemistry of speleothem records from southern Illinois: development of  $(^{234}\text{U})/(^{238}\text{U})$  as a proxy for paleoprecipitation. *Chem. Geol.* **221**, 1–20.
- Zongxing L., Qi F., Wang Q. J., Yanlong K., Aifang C., Song Y., Yongge L., Jianguo L. and Xiaoyan G. (2016) Contributions of local terrestrial evaporation and transpiration to precipitation using  $\delta^{18}\text{O}$  and D-excess as a proxy in Shiyang inland river basin in China. *Glob. Planet. Change* **146**, 140–151.

Associate editor: Jessica Tierney